Influence of substrate heating during deposition on the microstructure of thin polycrystalline gold films

Institute of Micro- and Nanostructure Research
Friedrich-Alexander-Universität Erlangen-Nürnberg
Prof. Dr. rer. nat. habil. Erdmann Spiecker

Bachelor Thesis

submitted by

Sophia Peters

Born: 28.09.2004 in Aachen

on

30.07.2025

Supervisor: M.Sc. Martin Dierner,

Prof. Dr. rer. nat. habil. Erdmann Spiecker

Abstract

This thesis investigates the microstructure of gold (Au) thin films on sapphire (α -Al₂O₃) and zinc oxide (ZnO) substrates at varying deposition temperatures (room temperature, 50 °C, 100 °C, 150 °C, 200 °C, and 250 °C). The study focuses on the evolution of film morphology and crystallographic texture dependent on the deposition temperature as well as the influence of the substrate.

At elevated substrate temperatures during e-beam deposition, the additional thermal energy provided to the atoms enables the film to grow in a more energetically favourable manner. This can, for example, lead to a significant increase in grain size and the development of a preferred crystallographic orientation. Gold (Au) films deposited on sapphire substrates tend to form a pronounced (111) fibre texture at higher temperatures. When deposited on ZnO, an additional in-plane orientation relationship (OR2) is favoured, indicating epitaxial growth which in turn, leads to abnormal grain growth. On the other hand, elevated substrate temperatures can also hinder nucleation and the coalescence of the film. The added thermal energy increases the critical size required for stable nuclei, which in turn raises the critical film thickness (thickness at which the film becomes continuous). This effect is particularly noticeable for Au films on sapphire. On ZnO, where the Au film is mostly closed also at higher deposition temperatures was associated to the strong orientation relation (OR2) between the film and substrate.

Additionally, post-annealing at 800°C for 5 minutes is performed to further investigate the influence of the as-deposited microstructure on that evolving at elevated temperatures. Interestingly, the initial deposition temperature of the thin film presents a significant influence on the microstructural evolution at 800°C. It was generally found that deposition at higher temperatures enhanced the thermal stability. The Au films on sapphire develop into nanoparticles via solid-state dewetting whereas the resulting particle size decreases and the particle density increases with increasing deposition temperature suggesting a correlation with the pre-existing voids in the as-deposited films. For Au films deposited on ZnO at substrate temperatures above 100 °C, which already exhibit epitaxial growth and abnormal grain growth in the as-deposited state, the film remains nearly continuous after post-annealing and maintains the OR2 orientation relationship. In contrast, films deposited at lower temperatures tend to break up during annealing and exhibit a (111) fibre texture. Furthermore, at a deposition temperature of 250 °C, a distinct dewetting mechanism is observed upon annealing at 800 °C: hole formation initiates at the film-substrate interface, and the displaced material accumulates on the surface in the form of hillocks.

Zusammenfassung

In dieser Arbeit wird die Mikrostruktur von Gold (Au) Dünnfilme auf Saphir- (α-Al₂O₃) und Zinkoxid- (ZnO) Substraten bei variierenden Abscheidetemperaturen (Raumtemperatur, 50 °C, 100 °C, 150 °C, 200 °C und 250 °C) untersucht. Der Fokus der Studie liegt auf der Entwicklung der Filmmorphologie und der kristallographischen Textur in Abhängigkeit von der Abscheidetemperatur sowie dem Einfluss des Substratmaterials.

Bei erhöhten Substrattemperaturen während der E-Beam-Abscheidung ermöglicht die zusätzliche thermische Energie, die den Atomen zugeführt wird, ein energetisch günstigeres Wachstum des Films. Dies kann beispielsweise zu einer deutlichen Vergrößerung der Korngröße sowie zur Ausbildung einer bevorzugten kristallographischen Orientierung führen. Goldfilme, die auf Saphir abgeschieden werden, zeigen bei höheren Temperaturen eine ausgeprägte (111) Fasertextur. Auf ZnO-Substraten wird darüber hinaus eine zusätzliche inplane Orientierungsbeziehung (OR2) bevorzugt, was auf epitaktisches Wachstum hinweist und wiederum zu abnormalem Kornwachstum führt. Erhöhte Substrattemperaturen können jedoch auch die Nukleation und das Zusammenwachsen des Films behindern. Die zugeführte thermische Energie erhöht die kritische Größe stabiler Keime, was wiederum zur Erhöhung der kritischen Filmdicke führt, also der Dicke, bei der der Film durchgehend ist. Dieser Effekt ist besonders bei Au-Filmen auf Saphir deutlich zu beobachten. Auf ZnO sind die Au Filme auch bei höheren Temperaturen noch überwiegend geschlossen, was auf die starke Orientierungsbeziehung (OR2) zwischen Substrat und Film zurückgeführt werden kann.

Zusätzlich wurde Post-Annealing bei 800 °C für 5 Minuten durchgeführt, um den Einfluss der anfänglichen Mikrostruktur auf die Entwicklung bei erhöhten Temperaturen weiter zu untersuchen. Interessanterweise zeigt sich, dass die Abscheidetemperatur des Dünnfilms einen signifikanten Einfluss auf die mikrostrukturelle Entwicklung bei 800 °C hat.

Es wurde allgemein festgestellt, dass eine höhere Abscheidetemperatur die thermische Stabilität der Filme erhöht. Die Au-Filme auf Saphir zersetzen sich im Zuge eines Solid-State Dewetting-Prozesses in Nanopartikel, wobei die resultierende Partikelgröße mit steigender Abscheidetemperatur abnimmt, und die Partikeldichte zunimmt. Dies deutet auf einen Zusammenhang mit bereits vorhandenen Löchern in den abgeschiedenen Filmen hin.

Für Au-Filme, die auf ZnO bei Substrattemperaturen über 100 °C abgeschieden wurden und bereits in diesem Zustand epitaktisches Wachstum sowie abnormales Kornwachstum zeigen, bleibt der Film nach dem Post-Annealing weitgehend zusammenhängend und behält die OR2-Orientierungsbeziehung bei. Im Gegensatz dazu brechen Filme, die bei niedrigeren Temperaturen abgeschieden wurden, während des Heizens auf und zeigen eine (111) Fasertextur. Darüber hinaus tritt bei einer Abscheidetemperatur von 250 °C ein veränderter Dewetting-Mechanismus bei 800 °C auf. Die Lochbildung beginnt an der Film-Substrat-Grenzfläche, und das verdrängte Material sammelt sich in Form von Hillocks an der Filmoberfläche an.

Contents

| 1 INTRODUCTION | 1 |
|--|----|
| 2 FUNDAMENTALS | 3 |
| 2.1 PHYSICAL VAPOR DEPOSITION OF THIN METALLIC FILMS | 3 |
| 2.1.1 Thin film growth | 3 |
| 2.1.2 Influence of the substrate temperature | 7 |
| 2.2 SOLID-STATE DEWETTING | 11 |
| 2.2.1 Mechanism | 11 |
| 2.2.2 Particle formation | 13 |
| 2.2.3 Related Processes | 15 |
| 3 MATERIALS AND METHODS | 16 |
| 3.1 E-BEAM EVAPORATION | 16 |
| 3.2 RAPID THERMAL ANNEALING | 18 |
| 3.3 AU ON SAPPHIRE AND ZNO SUBSTRATES | 19 |
| 3.4 CHARACTERIZATION METHODS | 21 |
| 3.4.1 Scanning Electron Microscopy & Electron Backscattered Diffraction | 21 |
| 3.4.2 Atomic Force Microscopy | 26 |
| 3.4.3 Scanning Transmission Electron Microscopy | 27 |
| 4 RESULT | 29 |
| 4.1 TEMPERATURE DEPENDENT MICROSTRUCTURE OF AS-DEPOSITED AU FILMS | 29 |
| 4.1.1 Au on sapphire | |
| 4.1.2 Au on ZnO | 33 |
| 4.2 MICROSTRUCTURE EVOLUTION AT 800°C | 37 |
| 4.2.1 Au on sapphire | 37 |
| 4.2.2 Au on ZnO | 39 |
| 5 DISCUSSION | 42 |
| 5.1 TEMPERATURE CONTROL DURING E-BEAM DEPOSITION | 42 |
| 5.2 INFLUENCE OF TEMPERATURE DURING E-BEAM DEPOSITION OF THIN AU FILMS | 43 |
| 5.3 Effect of post-annealing at 800°C on the microstructure of thin Au films | 50 |
| 5.3.1 Au on sapphire | 50 |
| 5.3.2 Au on ZnO | 54 |
| 5.3.3 Substrate reaction ZnO with Au thin film | 59 |
| 5 CONCLUSION AND OUTLOOK | 61 |
| REFERENCES | 63 |
| FIDESSTATI ICHE ERKI ÄRUNG | 69 |

1 Introduction

Gold thin films have long played a pivotal role in a wide range of electronic and photonic applications. Their popularity is not only due to gold's chemical stability and excellent conductivity, but also due to the versatility with which its physical and structural properties can be tailored. Crucially, many of the functional properties of these films, such as electrical resistance, optical absorption, or catalytic activity, are directly linked to their microstructure. Grain size, texture, crystallinity, and film continuity are not just incidental features, but central parameters that govern performance [1], [2].

Among the numerous deposition techniques available, electron beam evaporation stands out as a widely used and accessible method for fabricating polycrystalline gold films. However, the growth of thin films is a complex process influenced by a variety of parameters, one of the most critical being temperature. Substrate heating during deposition can significantly alter early-stage processes like nucleation, grain growth, and surface diffusion. Despite its widespread practical use, especially since most e-beam systems offer substrate heating as a standard option, there remains a lack of systematic studies investigating how substrate temperature during deposition affects the resulting microstructure of gold thin films experimentally [3], [4], [5], [6].

Solid-state dewetting (SSD) describes the thermally induced transformation of continuous thin films into discrete nanoparticles. This process is driven by the intrinsic metastability of polycrystalline metal films, which possess high surface and interface energies. When such films are heated to temperatures well below their melting point, they tend to minimize their total energy by breaking up into isolated particles via diffusion mechanisms while remaining in the solid state. While often regarded as an unwanted degradation phenomenon in thin film applications, SSD has gained considerable attention as a straightforward and scalable method for fabricating metal nanoparticles with tailored optical or catalytic properties [7], [8], [9], [10], [11].

Yet, controlling the dewetting outcome, especially with respect to particle size, density, and uniformity, remains challenging. While parameters like initial film thickness are known to influence the final particle dimensions, some studies also suggest that the microstructural characteristics of the as-deposited film, such as texture and grain size, can also play a crucial role [11], [12].

The aim of this work is to investigate the influence of substrate heating during e-beam deposition on polycrystalline gold films systematically. Therefore, 40 nm thick gold films are deposited on ZnO and sapphire substrates at RT, 50°C, 100°C, 150°C, 200°C and 250°C. To study the influence on the microstructural evolution at higher temperature, post-annealing at 800°C is performed on all samples.

In order to explore the impact of deposition temperature, the study begins with a discussion of the fundamental principles of thin film growth and solid-state dewetting. This is followed by an overview of the materials and methods employed, laying the groundwork for the presentation and evaluation of the experimental results.

2 Fundamentals

A fundamental understanding of thin film growth and evolution is crucial for investigating how processing parameters influence film properties. In particular, substrate temperature during deposition plays a key role in determining the microstructure of polycrystalline thin films [2], [13]. This section outlines the essential concepts that form the basis for analysing the impact of thermal conditions on the growth and transformation of gold thin films.

2.1 Physical vapor deposition of thin metallic films

Thin metallic films are widely used in electronic, photonic, and micromechanical devices, serving various functional purposes [2]. Different deposition techniques such as physical vapor deposition (PVD), chemical vapor deposition (CVD), and solution-based methods are available for fabricating these films. Each technique has specific advantages and limitations, and the choice depends on the materials involved and the intended application [4].

In this work, thin metallic films were deposited using PVD, specifically electron beam evaporation. Therefore, the following section presents the fundamental mechanisms and parameters governing thin film growth via PVD.

2.1.1 Thin film growth

Generally, film formation consists of the fundamental processes nucleation, coalescence and thickness growth (Figure 1).

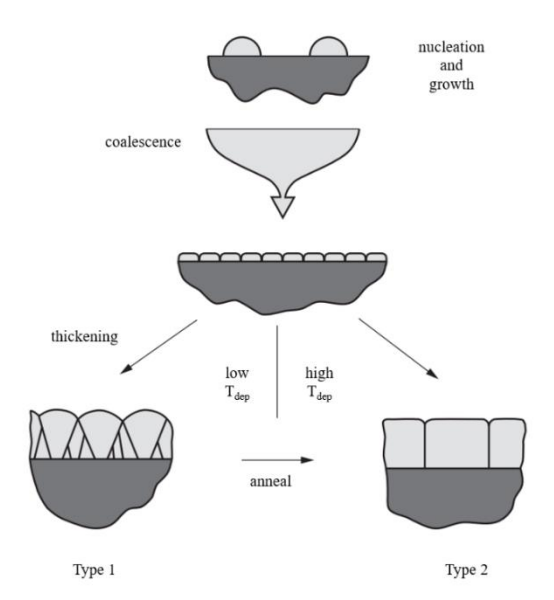


Figure 1: Fundamental processes nucleation, coalescence and thickening for thin film growth of polycrystalline thin films [2].

Nucleation

Nucleation marks the onset of thin film formation and refers to the agglomeration of adatoms into stable clusters. Initially, individual adatoms diffuse on the substrate and as they encounter

each other, they may form small clusters. These clusters can dissolve, but when they persist until reaching a critical cluster size a stable nucleus is formed. This critical cluster size is determined by a balance between the energy gain from creating a new phase and the energy cost associated with creating new surfaces and interfaces [2].

To describe this balance for the nucleation of thin films the capillary model is often employed [2]. Under the assumption that the nuclei are three-dimensional spherical islands with an isotropic surface energy, the equilibrium contact angle θ is given by Young's equation:

$$\gamma_{s} = \gamma_{i} + \gamma_{f} \cos(\theta) \tag{1}$$

with surface energy of the substrate γ_s , surface energy of the island γ_f and interface energy γ_i (Figure 2 a)).

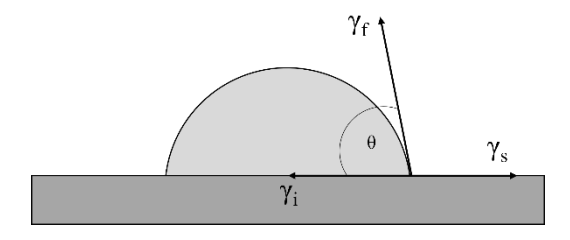


Figure 2: Island with an equilibrated contact angle θ for interface energy γi , surface energy γf and substrate surface energy γs after Young's equation (redrawn after [2])

The nuclei continue to grow as arriving adatoms are adsorbed. When they reach a cluster size where a defined crystallographic structure emerges, certain orientations that minimize the surface and interface energy of the island are preferred [2].

There are three different growth modes depending on the surface and interface energies of the substrate and the material that determine the morphology of the film (Figure 3). At the transition between nucleation and coalescence the growth mode of the film becomes apparent. The first mode is the Frank-van Merwe mode, where the film forms layer by layer. Second is the Volmer-Weber mode, where nuclei in form of separate islands form. Thirdly, a mix of both may occur when a few monolayers form at the interface and then islands grow on top (Stranski-Krastanov mode). For polycrystalline metallic thin films, the Volmer-Weber mode is typically observed, leading to the formation of separated islands in the early stages [13].

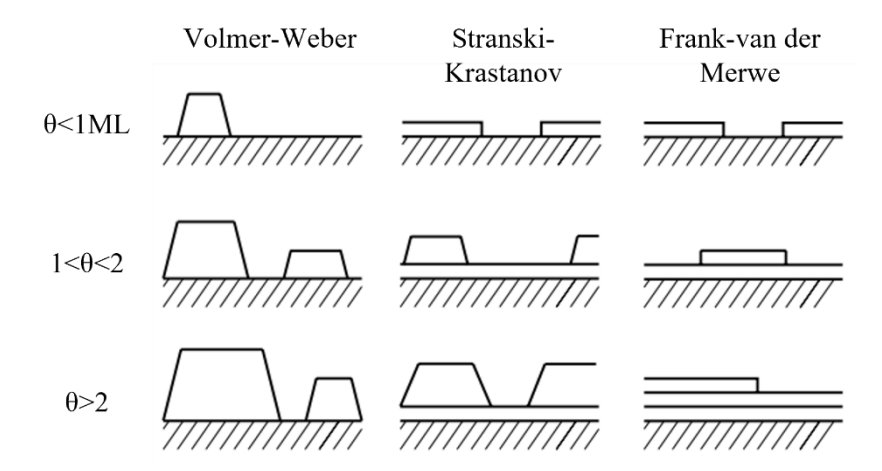


Figure 3: Nucleation growth modes for different surface coverages θ in monolayers (ML). From left to right, island growth (Volmer-Weber), layer plus island growth (Stranski-Krastanov) and layer by layer growth (Frankvan der Merwe) [45].

Coalescence

Coalescence describes the process when the separated islands have grown enough to contact an adjacent island. A grain boundary forms in between the islands as it has a lower energy than the surfaces of the two islands. If one of the islands is energetically unfavourable due to size or surface and interface energies, the more favourable island will grow on cost of the other (Figure 4). This coarsening process is dependent on the surface self-diffusion and the grain boundary self-diffusion but also on the energetic difference between the islands and the deposition rate. Therefore, it is possible, but not mandatory that smaller islands disappear during coalescence and the grain size increases. It was found that the typical (111) texture of gold thin films that is observed even at room temperature deposition can be due to grain growth during coalescence [2].

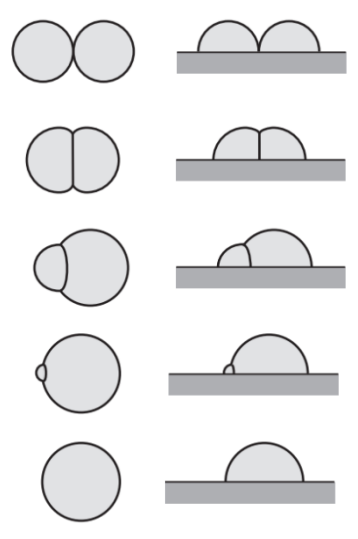


Figure 4: Grain growth during coalescence due to energetic differences of the islands [2].

Growth

When the islands are coalesced into a continuous network, the film has reached its critical thickness [13]. Then the thickness growth process of the film begins through epitaxial growth on already existing grains. The microstructural evolution of the film during this phase depends largely on the mobility of the gain boundaries.

If grain boundaries remain mobile during deposition, grain coarsening can continue as the film thickens, a behaviour characteristic of what is termed type 2 thickening. Conversely, if grain boundaries are immobile, the grains tend to grow vertically, resulting in structures with high aspect ratios; this is referred to as type 1 thickening (Figure 1) For polycrystalline gold thin films, type 2 thickening is expected. [2].

2.1.2 Influence of the substrate temperature

During thin film growth many processes are temperature-dependent leading to a significant influence of the substrate temperature on the microstructural evolution of the thin film [2]. The first temperature dependent process is the nucleation. The nucleation rate is given by

$$I = I_0 R^{n^*} \exp\left(\frac{-\Delta G_n^*}{kT}\right) \tag{2}$$

with the constant I_0 , Boltzmann constant k, substrate temperature T, deposition flux R, critical cluster size n^* and the energy required to form a cluster ΔG_{n^*} . This generally shows that the nucleation rate decreases with increasing temperature. However, when the temperature increases, the critical cluster size n^* and ΔG_{n^*} increase which means that the temperature dependence increases at higher temperatures [2].

Not only the nucleation rate but also the growth of the nuclei is dependent on temperature. When an island has formed it can grow by adding atoms that are deposited directly on the island or through adatoms deposited within the distance δ from the island on the substrate (Figure 5). The extent of the δ area depends on the mean residence time τ as well as the diffusivity for adatoms, both being functions of the temperature. With increasing temperature, δ can both increase or decrease depending on the relation between enhanced surface diffusion and desorption even though decreasing δ is often observed. Experimentally, it has been shown that nucleation stops when the δ areas cover the entire surface [2].

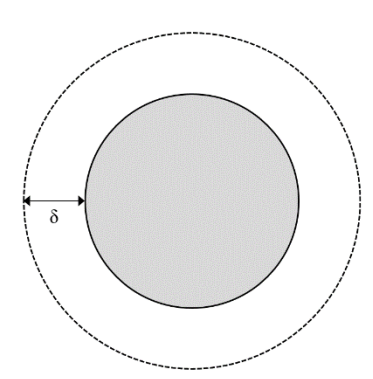
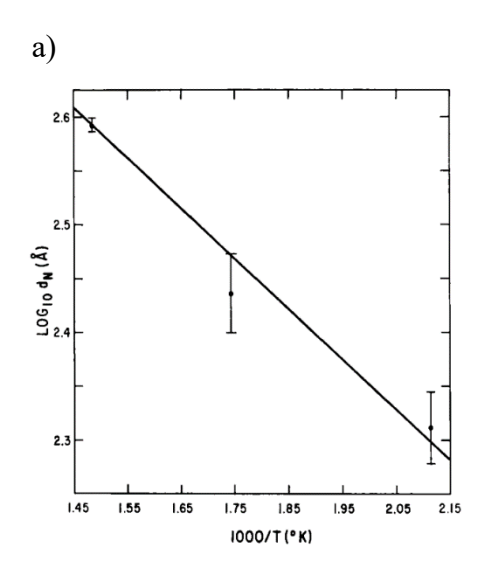


Figure 5: Island adsorbs atoms that are deposited directly on top of it or within the distance δ (redrawn after [2]).

For platinum, gold and silver deposited on rock salt and glass it was also observed that the island density decreases with increasing temperature (Figure 6 a)) [14], [15].

The grain size at impingement d_i is a function of the nucleation rate I and the δ area which are both functions of temperature leading to an increasing grain size at impingement with increasing substrate temperature. If d_i increases, consequently the film thickness at coalescence increases. This was confirmed by Chorpa et.al. [15] for silver on glass (Figure 6 b)) and also

by Golan et.al. [16] (gold on mica) where the film deposited at higher temperatures had elongated holes whereas the film deposited at room temperature was continuous [15], [16]. Not only the grain size at impingement but also grain growth during coalescence and thickening is expected to increase with increasing substrate temperature. Grain growth is dependent on grain boundary self-diffusion and surface self-diffusion which are both temperature-dependent. For normal grain growth, the mean grain size is not expected to become larger than three times the film thickness. However, if larger grains are observed, usually also much smaller grains are present leading to a bimodal grain size distribution [2], [16].



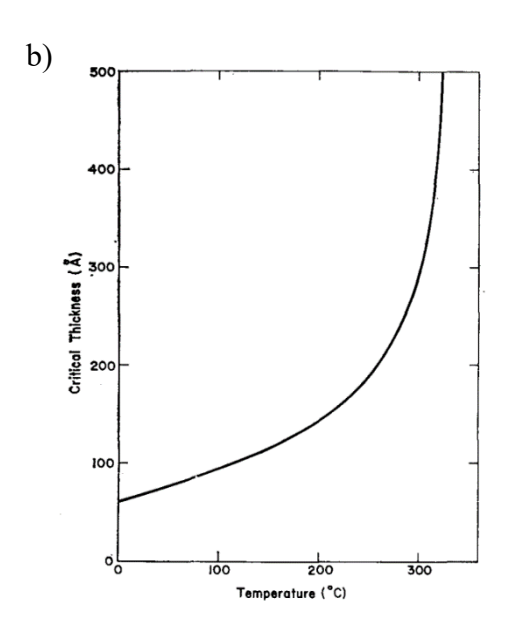


Figure 6: a) Experimental data for platinum deposits on rock salt by Sumner; Logarithm of island spacing d_n over reciprocal temperature. The island density decreases with increasing temperature therefore larger islands were observed [14], b) Experimental data from Chopra et.al.; critical film thickness over temperature for silver deposited on glass [15].

As the temperature influences many of the processes occurring during thin film growth, for the same material classes and homologues temperatures T_h (temperature divided by melting temperature) similar microstructures emerge. These typical microstructures were classified in so called zone models. The first zone model was discussed by Movchan and Demchishin in 1969 [17] and then further extended by Thornton in 1974 [18], Messier [19] and by Grovenor in 1984 [20]. The different extensions differ mainly in the parameters that are considered which is especially important for sputter deposition or transition structures in between zone 1 and zone 2. Nevertheless, they all agree in their main findings (Figure 7) [2], [13], [18].

The zone model consists of three zones. The first zone describes the microstructure at low homologues temperatures ($T_h < 0.3$) and is dominated by shadowing effects due to low surface and adatom diffusion. The shadowing leads to voided grain boundaries and a high surface roughness resulting from the initial nuclei and preferential growth similar to the type 1

thickening (c.f. Figure 1) discussed above. Zone 2 refers to homologue temperatures in the range of $0.3 < T_h < 0.5$. In this range surface diffusion is the dominant mechanism resulting in columnar grains and a smooth surface. The columnar grains grow by surface recrystallization and the crystallites grow in preferred orientations. Additionally, the surface is faceted and the grain diameter further increases with increasing substrate temperature. In the third zone that covers homologues temperatures of $0.5 < T_h < 1$, the microstructural evolution is mainly driven by bulk diffusion. The characteristic forms of appearance are large equiaxed grains and bright surfaces (Figure 7) [2], [13], [18].

However, it needs to be considered that the zone models are usually discussed for sputter deposition and for thick films. Therefore, the temperature ranges of the zones may vary as e.g., Sanders defines the first range as $T_h < 0.1$ and the second range as $0.1 < T_h < 0.3$ [2].

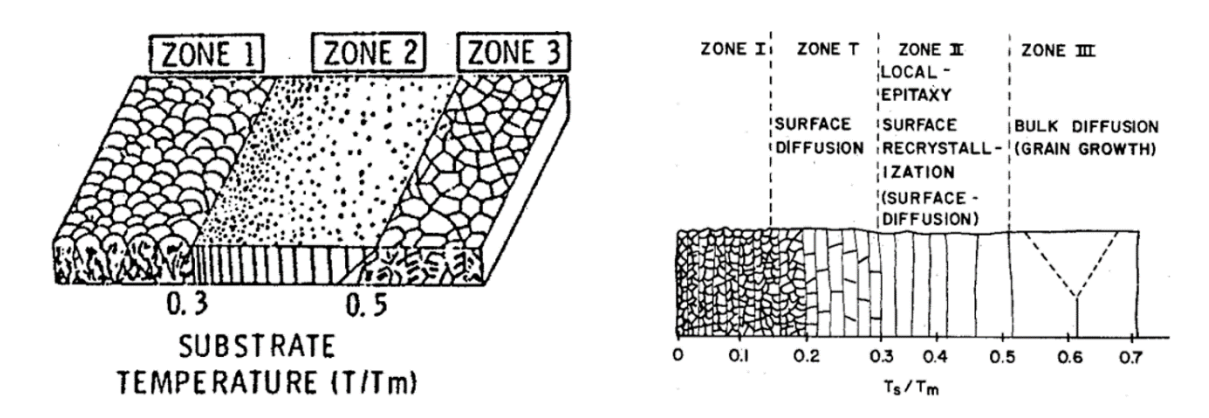


Figure 7: Schematic illustration of zone model of Movchan (left) and an extension with a transition zone T in between zone one and two by Thornton (right) [13].

A study from Lansaker et.al. [21] compared the effect of substrate heating during deposition with post-annealing at the same temperatures. Therefore, 5 nm gold were either sputtered on SnO₂ substrates at elevated temperatures or annealed after room temperature deposition.

The film is not closed at room-temperature deposition. In both experiment series, the consistency of the film decreases with increasing temperature. The structure yet differed quite a lot as the features of the post-annealed samples are a lot bigger compared to the samples deposited at the same temperature (Figure 8) [21].

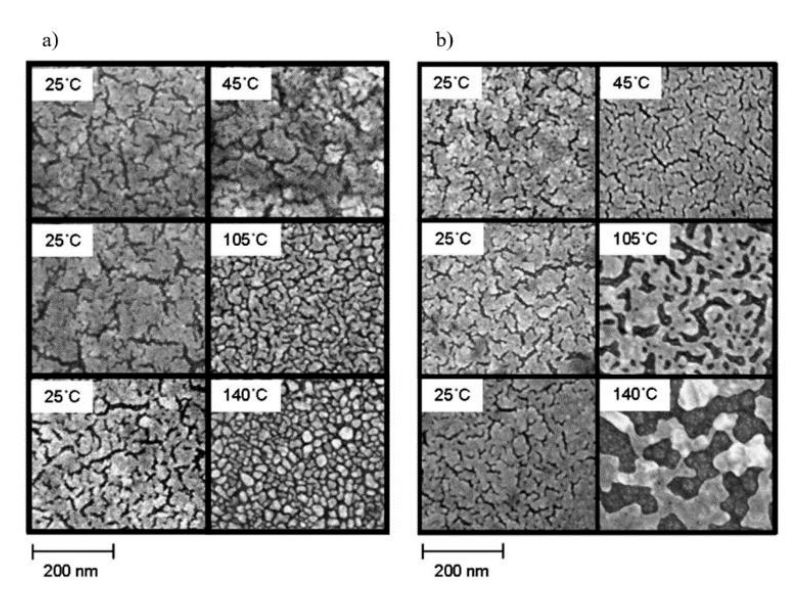


Figure 8: a) Au on SnO2 deposited at room temperature and at elevated temperatures b) deposited at room temperature and post-annealed [21].

2.2 Solid-State Dewetting

Due to their high surface to volume ratio thin films generally have very high surface energies which is why they are metastable. Hence, at elevated temperatures thin films undergo dewetting in the solid or crystalline state to reduce the system's total energy until equilibrated particles have formed - provided the temperature remains sufficiently high throughout the process [8].

2.2.1 Mechanism

Solid-state dewetting (SSD) typically initiates at pre-existing defects in the film, such as edges, grain boundaries, or voids. The dominant mass transport mechanism driving this process is surface self-diffusion. When SSD begins at a grain boundary, grooves form on the film surface due to atom diffusion away from the grain boundary (Figure 9 a)). This grooving process results in the formation of an elevated rim along the boundary. As atoms continue to diffuse outward, a void nucleates and then further expands. The material that diffuses away from the hole via surface self-diffusion forms an elevated rim around the hole. Consequently, a valley develops behind this rim. In Figure 9 b), the self-surface diffusion mechanism is similar to that in Figure 9 a) but initiates through edge retraction. The valley formed behind the rim leads to the so-called pinch-off process, whereby the film separates into a wire and a new edge, allowing the process to restart [8], [9], [10].

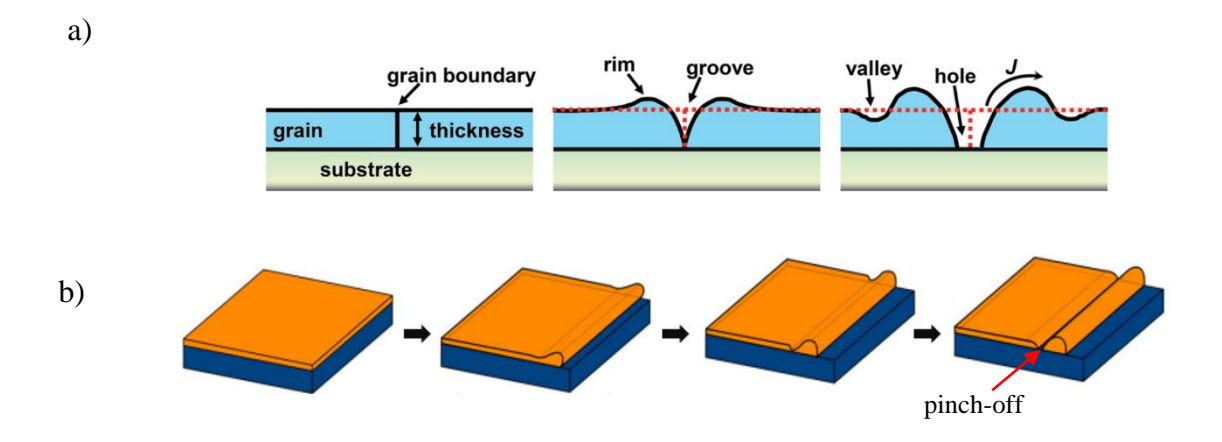


Figure 9: Solid-state dewetting mechanism a) through grain boundary grooving [9] b) begins with edge retraction and particle formation through pinch-off processes [10]

Nevertheless, holes in the film without surrounding rims have also been reported in various studies [22], [23], [24]. In these cases, so-called hillocks, agglomerates of material on the film surface, were observed, indicating the presence of an alternative dewetting mechanism. In various studies, different influencing factors have been proposed to explain the appearance of different dewetting mechanisms. Jacquet et al. [22] identified the atmosphere in which the samples were heated as a critical factor influencing the mechanism. Hillocks occurred in

oxygen-rich atmospheres [22]. In contrast, Shaffir et al. suggest that hillock formation occurs when the interfacial energy exceeds the surface energy. Under these conditions, voids tend to form at triple junctions at the interface rather than at surface grain boundaries (Figure 10 a)). The material then diffuses along the interface or along grain boundaries and accumulates at some distance from the nucleation site, forming isolated agglomerates (Figure 10 b)) [23], [24], [25].

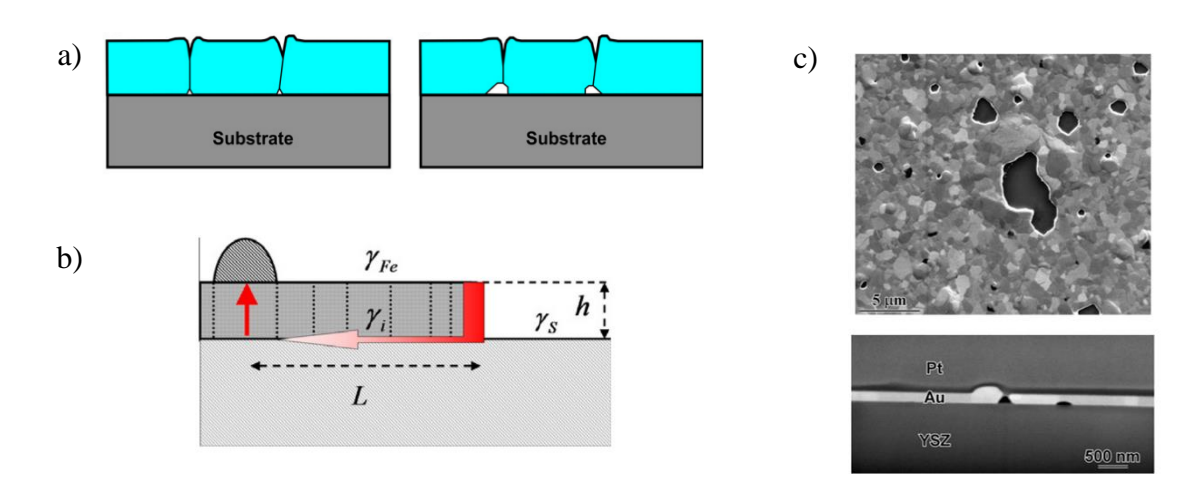


Figure 10: a) Schematic illustration of void formation at the interface of film and substrate [25] b) dewetting model for interface diffusion and hillock formation for iron on sapphire [23] c) experimental data from Shaffir etl.al. for Au on YSZ; holes without rims, hillocks and void formation at the interface was observed [24].

2.2.2 Particle formation

Regardless of which mechanism emerged in the early stages of the dewetting process, in the later stages the film is always separated into islands that then further evolve towards their equilibrium shape [25].

As the film retracts and voids expand, thin bridges of the material break apart leading to separation of neighbouring regions. The process finally results in isolated segments that subsequently evolve into compact particles as the system minimizes its surface and interface energy (Figure 11) [10].

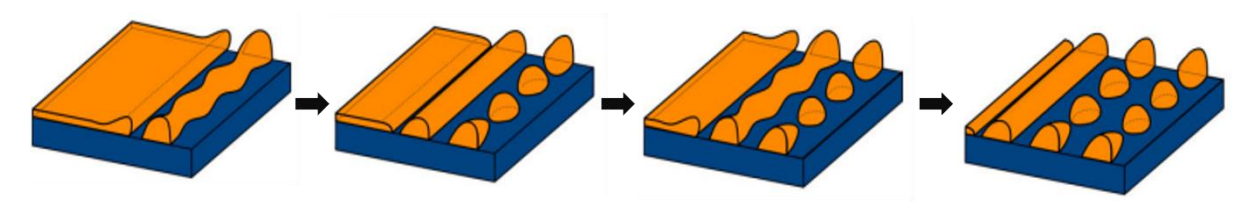


Figure 11: Pinch-off processes lead to the formation of wires which break apart into separated island that further evolve into equilibrated particles.

If the islands have an isotropic surface their equilibrium state would be described by Young's equation (equation 1) which was already discussed for the nucleation process. However, particles that have evolved out of a polycrystalline metallic thin film do have an anisotropic surface energy. Such equilibrium shapes are described by the Wullf construction and the Winterbottom construction which is an extension considering the interface energy between particle and substrate [25].

Figure 12 is a schematic two-dimensional Winterbottom construction for an equilibrated particle on a substrate. The vector γ_{hkl} represents the surface energy for the particular direction starting at the centre O, the so called Wullf point. The black continuous outline is the length of γ_{hkl} in every direction and the dashed hexagonal outline represents the equilibrium shape of the particle. Hence, only the crystallographic planes with the lowest surface energy are expressed resulting in the characteristic Wulff shape. For the Winterbottom construction the ratio of the surface and interface energies needs to be considered. The relation is given by

$$\frac{R_1}{R_2} = \frac{\gamma_i - \gamma_s}{\gamma_f} \tag{3}$$

where R_1 is the distance from Wulff point to substrate, R_2 the distance from Wulff point to uppermost particle facet, γ_i is the interface energy, γ_s is the surface energy of the substrate and γ_f is the surface energy of the uppermost particle facet) [25].

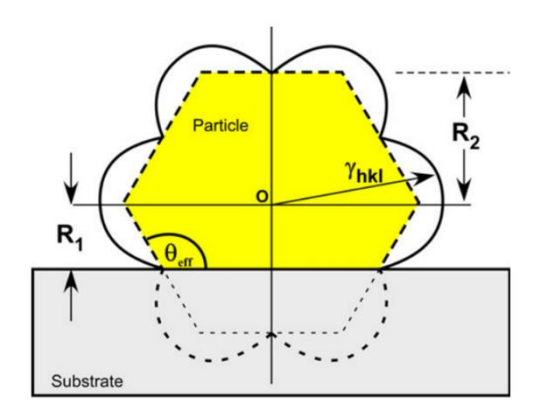


Figure 12: Illustration of a Winterbottom construction for an equilibrated particle on a substrate [25].

There are several parameters that influence the dewetting process and the particle formation. Generally, the choice of substrate and material, the film thickness and film morphology or the annealing parameters like temperature and annealing atmosphere [7].

It is often described in literature that there is a linear correlation between the mean particle size and the initial film thickness (Figure 13 a)) [7], [11]. However, the correlation between initial grain size and mean particle size has not been investigated in detail. Haustrup et.al. [12] have investigated the influence of different parameters like substrate choice, deposition temperature and film thickness of gold films on thin film growth and solid-state dewetting. They propose that with increasing initial mean grain diameter the mean nanoparticle diameter increases as well (Figure 13 b)). However, it should be considered that other factors, such as the substrate or film thickness, may have had a more dominant influence [12].

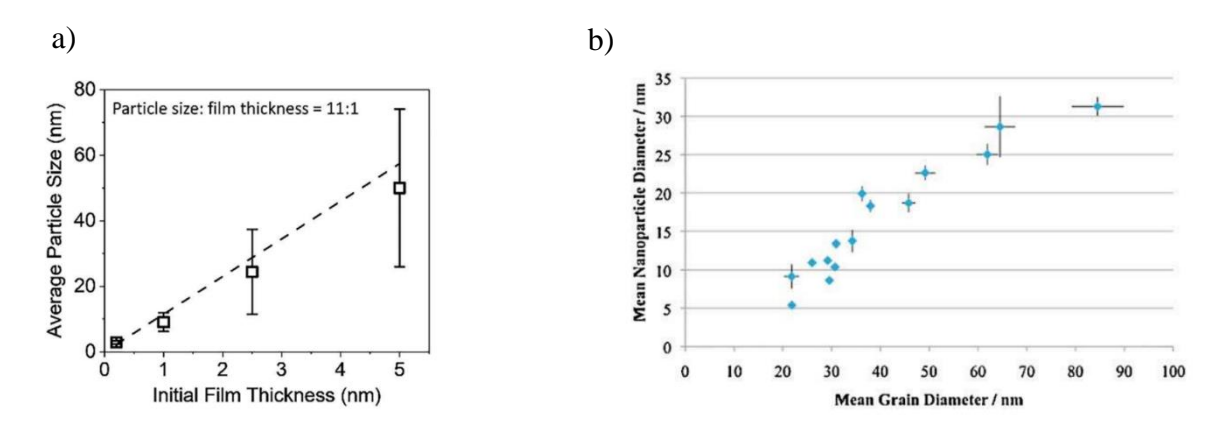


Figure 13: a) Experimental data for Pt particles on FTO: linear correlation between film thickness and particle size [11] b) Experimental data for Au on quartz, sapphire and silicon as well as different film thicknesses and deposition temperatures: particle size increases with increasing grain diameter [12].

2.2.3 Related Processes

At elevated temperatures SSD is not the only process that occurs to minimize the total energy of the system. Additionally, grain growth and texture evolution processes are observable [26]. Grain growth does not only occur at elevated temperatures during deposition but also during post-annealing processes as it reduces the energy by eliminating grain boundaries (Figure 14). Grain growth and SSD are competing processes, and one does not exclude the other. Therefore, grain growth may also influence the dewetting process. Furthermore, texture can decrease the energy as the out-of-plane and in-plane orientations influence the surface and interface energies. For fcc thin films like gold at elevated temperatures a strong (111) out-of-plane texture is observed [26], [27].

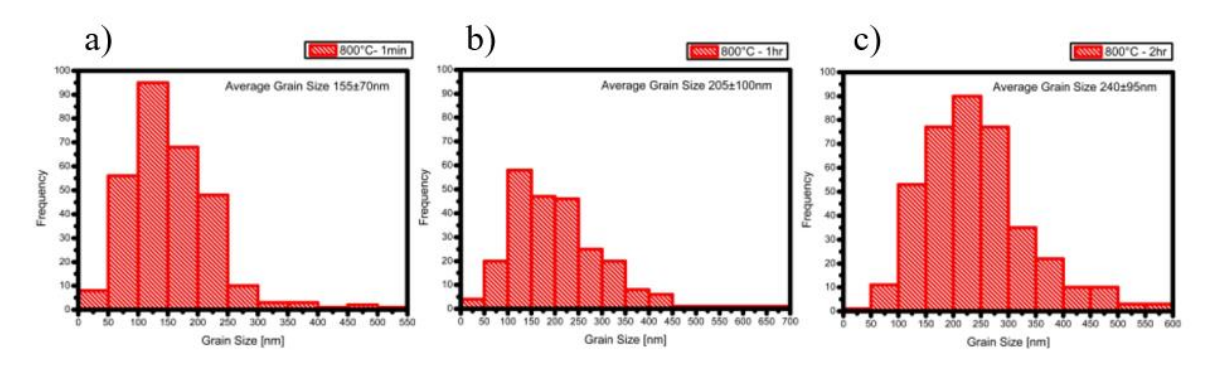


Figure 14: Grain size distributions of Pt film on sapphire annealed at 800°C for a) 1 minute b) 1 hour c) 2 hours [26].

Just like for thin film growth at elevated temperatures it is likely that grains with a preferred orientations grow on cost of grains that are energetically unfavourable. Atiya et.al. also observed abnormal grains at the edges of holes and that these holes did not continue to expand. It was suggested that grains that are energetically favourable stop the dewetting locally and then grow into abnormal grains (Figure 15) [26].

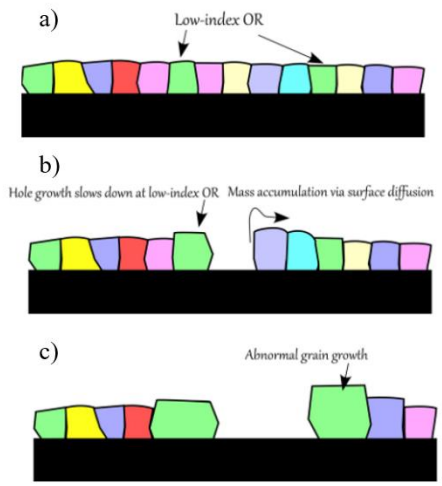


Figure 15: Schematic illustration of abnormal grain growth of low index OR grains adjacent to holes [26].

3 Materials and Methods

In this part the experimental methods and the material systems used in this work will be presented.

3.1 E-Beam Evaporation

Electron beam evaporation is a physical vapor deposition (PVD) technique widely used to fabricate high-purity thin films, offering precise control over material deposition and film thickness. This method utilizes a focused beam of high-energy electrons to heat and evaporate target materials under vacuum conditions. Electron beam evaporation can heat the target material up to 6000 °C making it suitable for a large variety of materials [3].

In Figure 16 a schematic of the deposition process is illustrated. To prevent contamination the filament is typically located next to or underneath the water-cooled crucible. Electrons are emitted by applying a low voltage but high current to the filament. The emitted electrons can be bundled through a cathode and accelerated through an anode. A magnetic field deflects the electron beam on the target material under an angle of 270° or 180° degree depending on the set up. When the electrons reach the material source different interactions take place including backscattered electrons or X-rays. Nevertheless, a large part of the kinetic energy of the electrons is converted to heat, melting and evaporating the target material locally. This is why sweep coils are used not only to focus the beam on the target but also to move it around the surface to provide a larger area and enable a more even evaporation. The substrate holder is located above the crucible so the evaporated atoms can be deposited on the substrate [3].

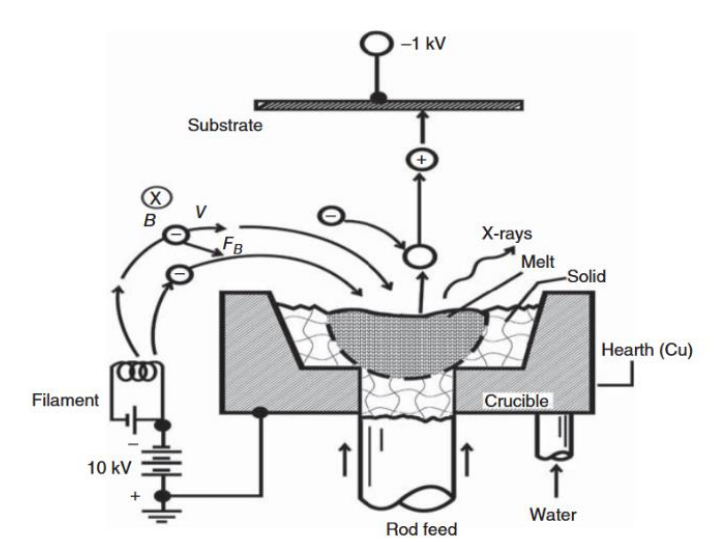


Figure 16: Schematic set up for electron beam evaporation deposition. Electrons are emitted by the filament and accelerated on the target material leading to evaporation of atoms or ions which then can be adsorbed on the substrate surface [3].

In this work an E-Beam PVD HVB 130 by Winter Vakuumtechnik is used. The vacuum during deposition was always below 2×10^{-5} mbar. The integrated substrate heater enables deposition

at elevated temperatures up to 250 °C whereby the thermocouple is placed directly underneath the substrate holder. The samples are produced in six batches, in each batch two sapphire and two ZnO substrates, so there is one sample for the as-deposited state and one that can be used for post-annealing. The first batch is deposited at room temperature (~20 °C) the following at 50 °C, 100 °C, 150 °C, 200 °C and 250 °C. The target temperature is set prior to deposition and kept constant during the deposition of the 40 nm gold.

3.2 Rapid Thermal Annealing

For the post-annealing step the samples are heated with a rapid thermal annealer (RTA), a AS-One 100 Rapid Thermal Processor by ANNEALSYS. The RTA enables heating rates of up to 200 °C per second and can reach temperatures up to 1250 °C. As the RTA is designed for silicon wafers, the sample is placed on a silicon nitride wafer which is hold by quartz pins as shown in Figure 17. The infrared halogen lamp furnace is located above the wafer and the temperature is controlled by the pyrometer under the hole in the bedplate. If fast cooling is requested the wafer can be dropped on the water-cooled bedplate [28].

In this experiment all samples are annealed at 800 °C for 5 minutes in nitrogen atmosphere with a gas flow of 2000 sccm. After annealing the samples are cooled by fast-cooling. Before the annealing starts, the chamber is flushed with argon and pumped three times to minimize remaining air and insure an inert atmosphere during the annealing process. Furthermore, to preclude variations all samples are annealed in one batch. During and after cooling no further post-processing is performed.

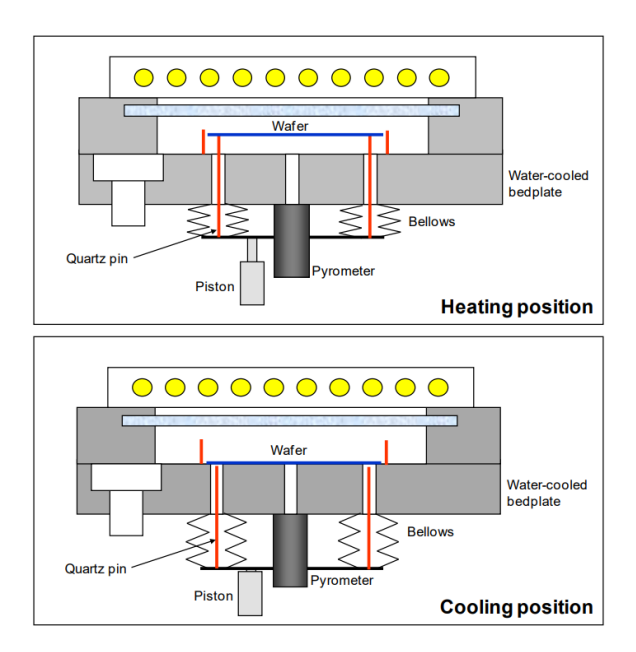


Figure 17: Schematic set up of RTA chamber for heating and fast cooling. A silicon wafer is hold by quartz pins, the halogen lamp furnace is located above and the pyrometer for temperature control underneath [28].

3.3 Au on sapphire and ZnO substrates

The substrates that are used are manufactured by CrysTec (Germany). The sapphire (α -Al₂O₃) substrates are 5×5 mm in length and width, 0,5 mm thick and have a (0001) orientation with K < 0,1 °. The substrates are polished on one side whereupon the gold is deposited on this side. The ZnO substrates are 5×5 mm in length and width, 0,33 mm thick and have a (0001) orientation. The ZnO is also polished on one side, the polar Zn-ZnO side, which is used to deposit the gold film on top.

Gold thin films can be used in various technological applications, such as plasmonics or sensing. Gold crystallizes in a face-centred cubic (fcc) structure and often exhibits a (111) texture if the substrate does not dictate something else (Figure 18). The surface energy of the (111) surface of gold is 1,238 J/m² [29]. However, the microstructure of gold thin films is dependent on the substrate [1], [16], [30].

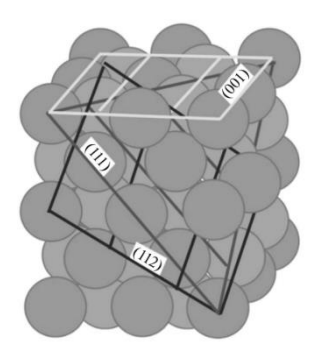


Figure 18: fcc structure with planes with high atomic density (111), (100), (112) [30].

The gold on sapphire system is frequently reported in literature. For (0001) sapphire a preferred (111) texture is often observed and becomes more pronounced at higher temperatures or by using a seed layer. Epitaxy does not occur unless an interlayer is present [31]. When gold nanoparticles are produced via SSD the equilibrated particles are highly faceted, single crystalline and the uppermost facet is most likely to be (111) oriented (Figure 19). The interface energy of (111) textured equilibrated gold particles on sapphire is 2,15 J/m2 [32]. However, if the particles are not equilibrated, they are still faceted but elongated and may feature grain boundaries [30], [31], [33], [34].

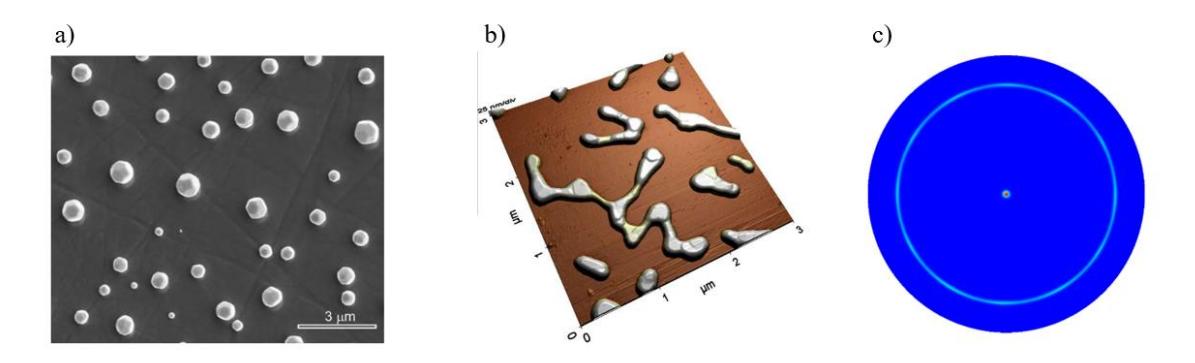


Figure 19: a) SEM image of equilibrated gold particles on sapphire annealed at 1000 °C for 100 h [32] b) AFM measurement of gold particles with grain boundaries that produce surface step [33]s c) (111) pole figure of gold on sapphire [34].

Zn-ZnO substrates in contrast to sapphire have a polar surface. The gold film presents a (111) texture out of plane on ZnO as well but, unlike sapphire, on ZnO epitaxy occurs at elevated temperatures. Firstly, an alignment of $<110>_{Au}$ || $<10\overline{1}0>_{ZnO}$ occurs which is in literature referred as orientation 1 (OR1). Orientation 2 (OR2) is 30° rotated and is the alignment of $<110>_{Au}$ || $<11\overline{2}0>_{ZnO}$ Dierner et al. [35] investigated the texture evolution of gold thin films on Zn-ZnO. In the as-deposited state a (111) fibre texture is observable as well as a slight tendency towards OR2. After annealing at 600 °C for 30 minutes OR1 and OR2 are present even though OR2 is more dominant. However, some OR1 grains are conspicuous large compared to grains with OR2. The sample that was annealed at 800 °C for 2 minutes differs significantly as there are very large grains indicating abnormal grain growth and OR1 is exclusively present (Figure 20).

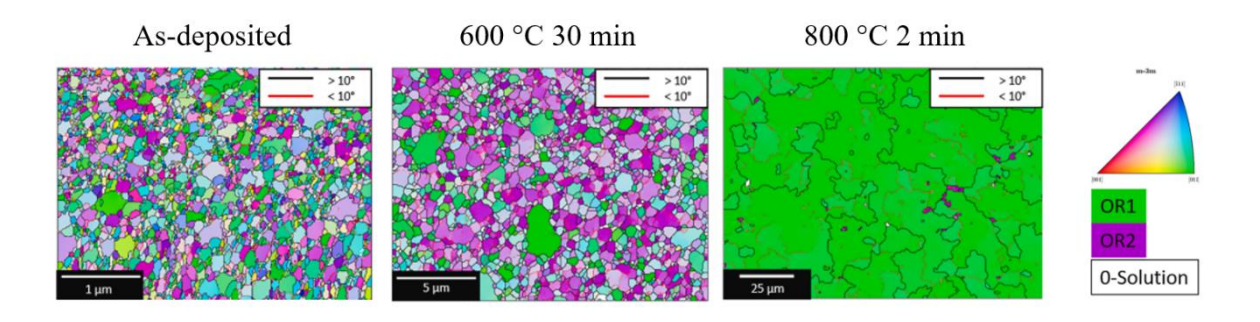


Figure 20: EBSD maps of Au films on polar Zn-ZnO substrate. As-dep. and annealing at 600°C have tendency to OR2 whereas annealing at 800°C leads to expressed OR1 [35].

3.4 Characterization methods

To investigate the samples different characterization methods are used. Scanning electron microscopy (SEM) provides information about the surface and the microstructure as well as grain size and texture especially in combination with electron back scattered diffraction (EBSD). Atomic Force Microscopy (AFM) furthermore can quantify the size and depth of the features and lastly scanning transmission electron microscopy (STEM) provides high resolution information and is used for the characterization of cross-section lamellas. Furthermore, energy-dispersive X-ray spectroscopy (EDX) can be used for chemical analysis.

3.4.1 Scanning Electron Microscopy & Electron Backscattered Diffraction SEM

SEM is a widely used characterization technique for investigating sample surfaces at the nanometre scale. The electron beam is focused onto the sample surface by a series of lenses and scanned point by point across the specimen using a deflection system. During this process, various interactions between the probe and the sample occur, which are detected by different types of detectors, resulting in the formation of a detailed image [36].

The setup of a SEM is illustrated in Figure 21. Firstly, electrons are emitted by an electron gun which in modern instruments are mostly field emission sources. The electron beam is accelerated toward the anode and formed by electromagnetic lenses. The condenser lens forms a parallel beam, and the objective lens focusses the beam into a probe on the sample surface. Apertures can be used to block scattered electrons and limit spherical aberrations, and the scan coils scan the electron probe over the specimen. In the specimen chamber the specimen is mounted on the stage and different detectors are fixed or can be inserted. Generally, high vacuum is required in the column and the chamber [36].

Figure 22 shows the possible interactions of the electron probe with the sample. Essentially, the secondary electrons (SE) and backscattered electrons (BSE) are important for imaging. Secondary electrons have a lower energy which is why they can only escape the material and reach the detector if they are generated close to the surface. This is why, in the SE mode the surface topography is visible. Backscattered electrons have a higher energy so they can come from deeper areas underneath the surface. The BSE mode provides a mix of compositional and topographic information. Atoms with a higher atomic number lead to a stronger backscattered signal leading to a strong material contrast when imaging with BSE (Z-contrast). Additionally, the BSE yield is dependent on the orientation of the crystal leading to the so-called channelling contrast. Therefore, different materials but also different grains can be visible in the BSE mode [36], [37].

In this work, for imaging a Zeiss GEMINI SEM 560 is used. Prior to imaging, the samples are cleaned using a built-in plasma cleaner. Imaging is carried out with an acceleration voltage of 2 kV and a working distance of 2 mm.

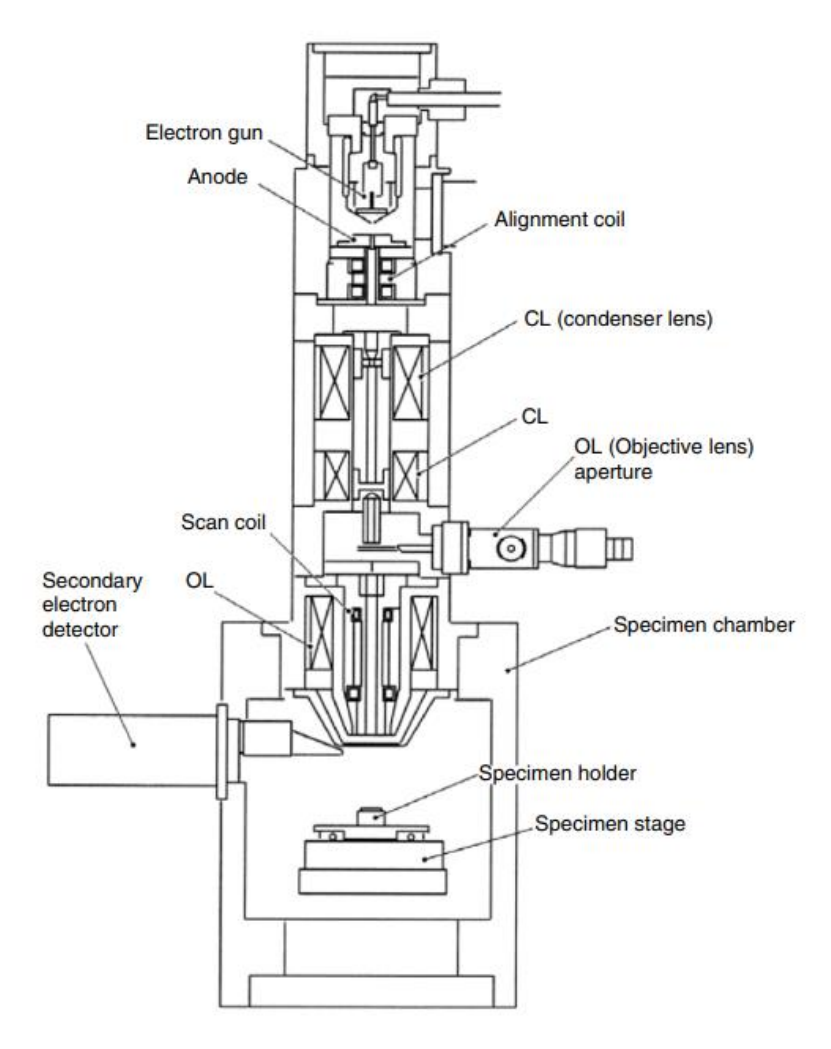


Figure 21: Schematic illustration of a scanning electron microscope. The electron beam is generated, formed by several lenses and scanned by coils. The detectors are located in the specimen chamber [36].

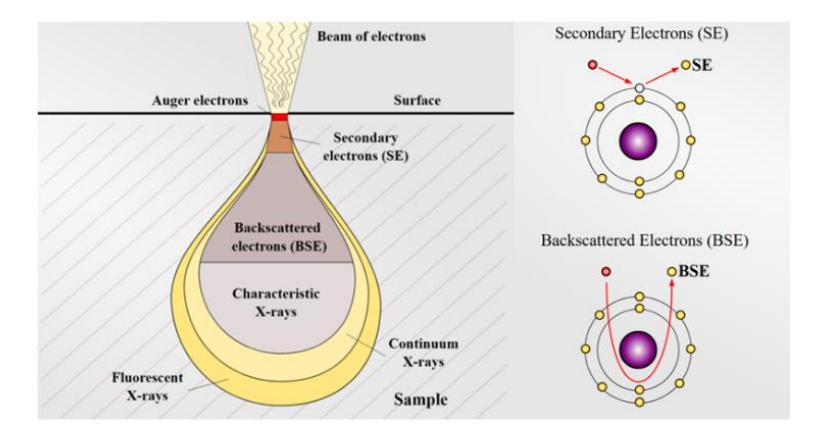


Figure 22: Schematic illustration of signals generated by electron probe by interacting with the material. Secondary electrons that can be detected are generated close to the surface; however backscattered electrons can come from deeper areas [49].

EBSD

EBSD is a powerful technique to analyse the crystallographic orientations of a polycrystalline film. The sample is tilted to 70° and an acceleration voltage of 10 kV is used. A direct detection EBSD camera (Clarity Super, Ametek GmbH) is utilized for the measurements. The size of the area and step size for the measurement are varied depending on the expected grain size for each sample estimated beforehand by SEM imaging.

When an electron beam strikes a crystalline solid, it scatters in all directions, but some electrons are scattered at the crystal planes at specific angles that comply with the Bragg equation:

$$\lambda = 2 \cdot d_{hk1} \cdot \sin(\theta) \tag{4}$$

with wavelength λ , spacing between lattice planes d, and the angle between incident beam vector and lattice plane θ (Figure 23 a)). Considering all vectors with an angle θ they form two opposing cones normal to the crystal plane which are the so-called Kossel cones (Figure 23 b)). On a screen these Kossel cones are visible as lines that are called Kikuchi lines and since there are always two cones, Kikuchi lines always appear in pairs, which is why they are also referred to as Kikuchi bands. Figure 23 c) schematically illustrates the overall setup in the SEM. As the angle θ is typically very small and the detector only captures a small section of the Kossel cone, the Kikuchi bands appear as straight lines on the detector, although they actually follow a parabolic shape, as shown in Figure 23 b) [38].

The angular spacing between these lines is two times the Bragg angle and thus proportional to the interplanar spacing of the crystal (see equation 4). Each pair of Kikuchi lines, or Kikuchi band, corresponds to a specific crystallographic plane. The intersections of multiple bands indicate zone axes, and the pattern reveals the crystal's angular relationships, including its symmetry [39].

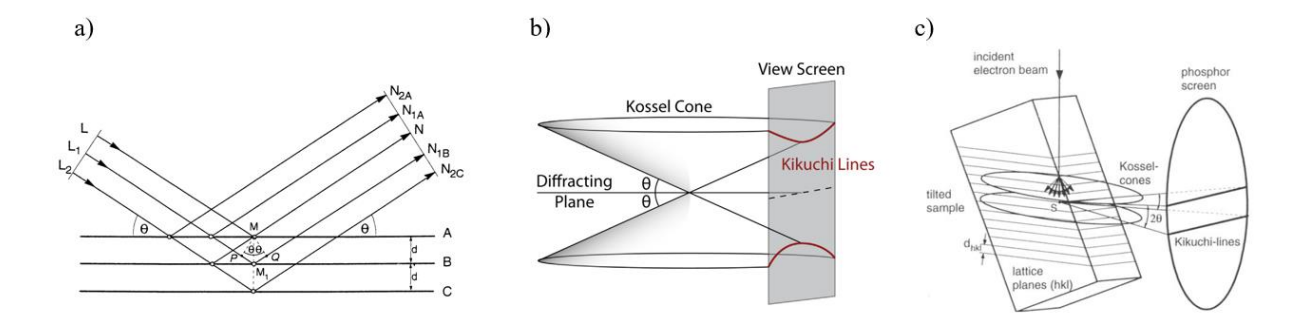


Figure 23: a) Bragg diffraction at lattice planes b) formation of Kossel cones [50] c) formation of Kikuchi-lines [39].

EBSD on, especially as-deposited thin films can be challenging with conventional indexing like Hough Indexing (HI), due to very small grains and a slight topography. The recorded data

in this thesis is indexed using the spherical indexing (SI) method which is a modern approach for determining crystal orientations from EBSD [39]. It utilizes the mathematical formalism of the spherical harmonic transform (SHT) to represent EBSD patterns as continuous functions on a unit sphere. Given an EBSD pattern $f(\theta, \phi)$ where θ and ϕ are the polar spherical angles, the pattern is expanded into a series of spherical harmonics $Y_m^l(\theta, \phi)$ forming an orthonormal basis on the sphere:

$$f(\theta, \phi) = \sum_{l=0}^{\infty} \sum_{m=-l}^{+l} \hat{f}_{l}^{m} Y_{m}^{l}(\theta, \phi)$$
 (5)

Here, \hat{f}_{l}^{m} are the complex coefficients that capture the spatial frequency content of the pattern. This decomposition allows for efficient and accurate comparison between the experimental pattern and a database of simulated Kikuchi patterns, each represented in the same harmonic space. Figure 24 a) shows a simulated Kikuchi pattern for gold at 10 kV. The Kikuchi pattern in c) is the experimental measured pattern and b) is the best match from the comparison of the SHT functions of the experimental and simulated pattern. Therefore, SI is a highly accurate approach that identifies the orientation rapidly compared to the dictionary indexing (DI) approach [39], [40], [41].

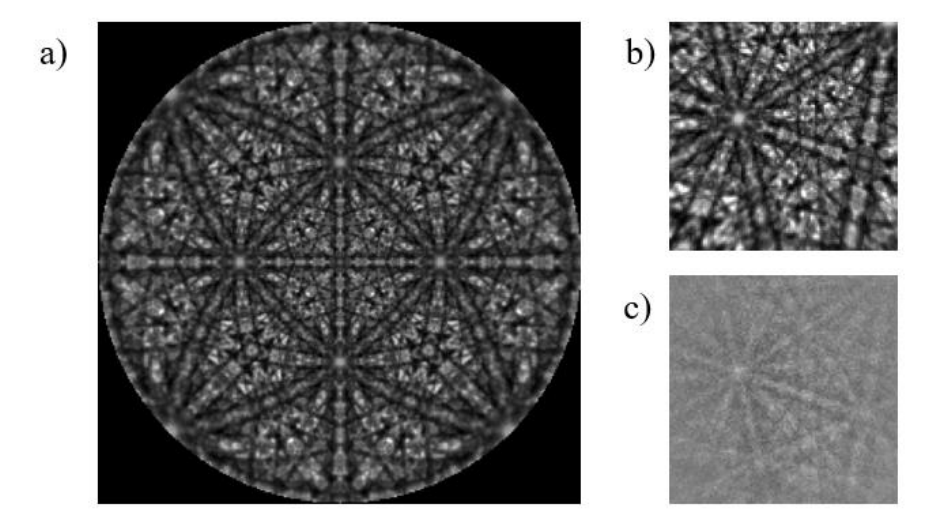


Figure 24: Kikuchi-pattern Au 10 kV a) simulated pattern b) and c) matched simulated and experimental pattern through spherical indexing.

A common method for texture representation is the use of pole figures. To represent a crystal plane, the intersection of the normal vector with a unit sphere is determined. This point is referred to as a pole. The sphere with the poles is then mapped onto a plane using a stereographic projection. The process works by positioning a virtual light source Q beneath the sphere, which then projects the poles onto the plane (Figure 25 a)). If the poles are evenly distributed, this indicates the absence of a preferred orientation (Figure 25 d)). If many poles cluster in a specific area, a preferred orientation is present. For example, in a {111} pole figure all poles represent (111) planes. If all poles are located around the centre of the pole figure it shows that the crystals preferably exhibit (111) planes parallel to the surface which is referred as fibre texture (Figure 25 b)). If a preferred in plane orientation (epitaxy) is present as well the poles form clusters at the outside of the sphere (Figure 25 c)) [42].

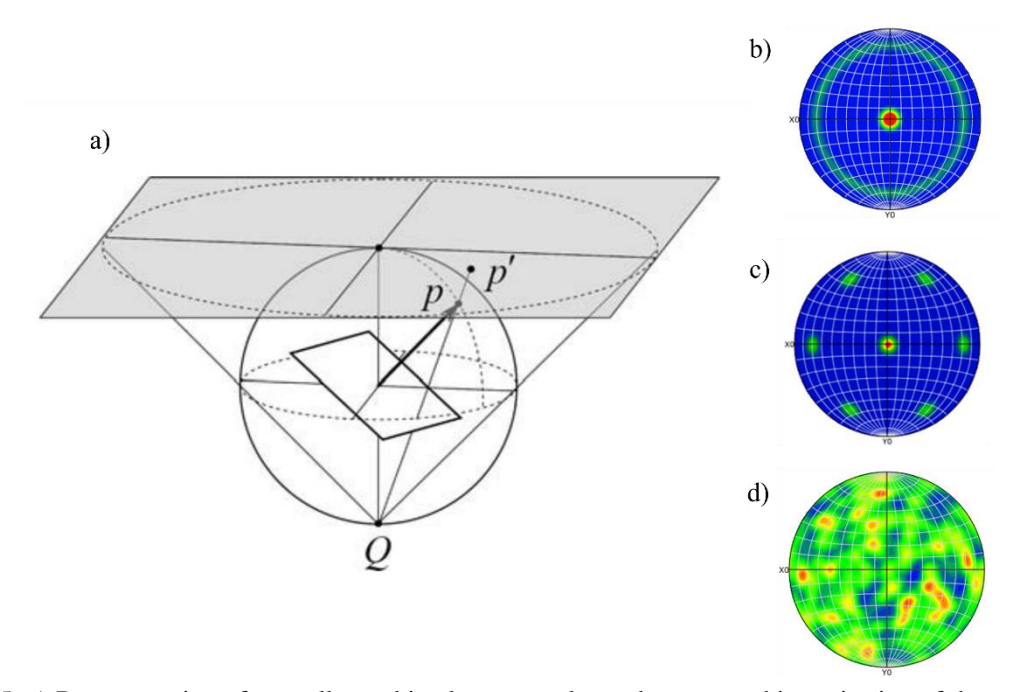


Figure 25: a) Representation of crystallographic planes as poles and stereographic projection of the unit sphere [42], (111) pole figures with b) fiber texture c) epitaxy d) random orientation.

3.4.2 Atomic Force Microscopy

Atomic force microscopy is a general term for methods that rely on an atomic force sample-probe interaction. It can be used to investigate the topography of a sample but also for electrical, optical, magnetic and mechanical properties. In this work AFM is used to investigate the topography of the samples quantitatively [43].

The general set up is illustrated in Figure 26. In this case the cantilever oscillates in the z-direction usually through a piezo. For scanning the sample is moved relative to the stationary tip but it is also possible that the tip scans over the stationary sample. To control the position of the cantilever an optical system is used and connected through a feedback loop [44], [45].

The AFM can be operated in the contact mode where the tip and the sample are constantly in contact or in the tapping mode. In this mode the cantilever oscillates in the z-direction at its resonance frequency and taps along the surface. Additionally, AFM can be performed in different environments like gas, liquid, ambient and vacuum depending on the application [44].

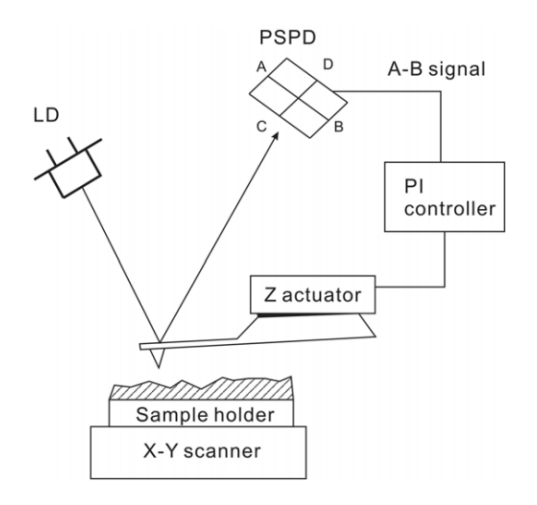


Figure 26: Schematic illustration of an AFM set up. A cantilever scans the sample recording the topography [45].

In this work a Park System NX10 AFM is used. The AFM is operated in ambient atmosphere in the tapping mode. The Z-scanner has a resolution of 0,015 nm and the XY-scanner has a resolution of 0,05 nm. The tip has a radius of 8 nm limiting the lateral resolution. The amplitude, scanning area and frequency are varied depending on the expected vertical and lateral feature size of the sample.

3.4.3 Scanning Transmission Electron Microscopy

In a scanning transmission electron microscope (STEM), a thin specimen is irradiated by an electron beam accelerated at a voltage typically ranging between 100 and 500 kV. In this work a Thermo Fisher Scientific Spectra 200 C-FEG TEM is used operating at 200 kV. The high acceleration voltages result in short electron wavelengths, enabling a resolution well below one nanometre. To allow electrons to pass through the specimen, it must generally be thinner than 100 nm [38].

In STEM, an electron probe with a diameter of approximately 0.2–5 nm is generated. The electron beam scans the specimen in a raster pattern and collects signals point-by-point, similar to SEM. STEM offers the advantage of simultaneous signal collection and enables high-resolution imaging of the crystal lattice [38].

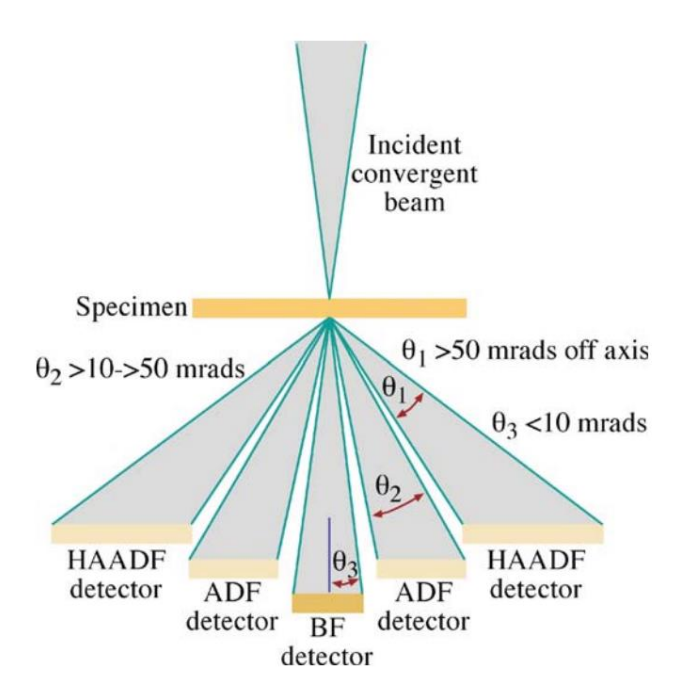


Figure 27: Detector set up in STEM. Electron beam forms a small probe and scans the sample. The detectors are arranged in annular geometry collecting signal from electrons that are scattered at different angles [38].

Figure 27 shows the typical detector set up for STEM. The contrast mechanism arises from the dependence of electron scattering on the atomic number of the elements in the sample. Heavier atoms, with higher atomic numbers, scatter incident electrons more strongly and at larger angles compared to lighter elements (Z-contrast). To exploit this effect, detectors are arranged in annular geometries that are sensitive to different scattering angles [38].

The Bright-Field (BF) detector primarily collects electrons that have undergone little to no scattering. In contrast, the High-Angle Annular Dark-Field (HAADF) detector captures electrons scattered at high angles, where the intensity of the scattered signal scales

approximately with the square of the atomic number ($\propto Z^2$), making HAADF imaging highly sensitive to compositional variations at the atomic scale [38].

Consequently, BF and HAADF images are complementary: features that appear bright in BF images tend to appear dark in HAADF images, and vice versa.

EDX

Energy dispersive x-ray (EDX) spectroscopy is a valuable technique for the chemical analysis of specimens. Characteristic x-rays are produced as a secondary emission resulting from the interaction between the incident electron beam and the atoms within the specimen. When an atom is ionized by the electron beam, an electron from a higher energy shell transitions to fill the resulting vacancy in an inner shell. This electronic transition leads to the emission of characteristic x-rays with energies specific to the element involved. These x-rays can be detected, and the energy and intensity of the corresponding peaks in the spectrum provide both qualitative and quantitative information about the chemical composition of the specimen.

Since characteristic x-rays are generated whenever the electron beam energy is sufficient to ionize the atoms, EDX is extensively employed in STEM as well as SEM [46].

4 Result

In this part the experimental results will be presented.

4.1 Temperature dependent microstructure of as-deposited Au films

This study investigates the influence of substrate temperature during the deposition of thin films, revealing a significant dependence of the microstructure of gold thin films on sapphire and ZnO substrates, especially regarding the grain structure and texture. To examine this relationship in detail, a series of measurements were conducted, the results of which are presented in the following sections.

4.1.1 Au on sapphire

Grain structure

Figure 28 a) presents SEM images of 40 nm thick Au films deposited on sapphire substrates at various temperatures. Each image consists of a split view, combining secondary electron (SE) and backscattered electron (BSE) imaging taken at the same location.

At room temperature (RT), the SE image reveals a rough surface topography characterized by small, similarly sized features. These structures initially appear to resemble small grains. However, the corresponding BSE image provides a clearer distinction between surface topography and the actual grain structure. The BSE image reveals the presence of both large and small grains, indicating that the observed features in SE mode primarily reflect surface topography rather than true grain boundaries. In BSE mode, the polycrystalline nature of the film becomes evident, showing a mixture of very small grains, some of which are difficult to distinguish individually and significantly larger grains, several times the size of the smaller ones. The microstructure of the Au film deposited at 50 °C already exhibits notable differences compared to the film deposited at RT. In SE mode, the surface features appear generally larger, and unlike the RT sample, they also vary more significantly in size. Additionally, small spherical structures, around 10 nm in diameter, are observed atop the grain-like surface features. The BSE image suggests that some of these larger surface features correspond to individual grains. However, certain large grains still exhibit multiple surface features, but larger surface structures tend to form on larger grains. Overall, the film contains a higher number of large grains, many of which are larger than those in the RT sample, and a reduced number of small grains. At a deposition temperature of 100°C the surface structures look similar to those that are observable in the 50°C sample. Comparing the SE and BSE image, the larger surface structures in the SE image seem to be identical to the different grains in the BSE image. The grain size increases compared to deposition at 50°C and there are significantly more large grains and less small grains. Additionally, the film is not closed as some small round or slightly elongated holes are observable along the grain boundaries. There are more of the small spherical structures on top of the grains in the SE image and some grains are fully covered with

them. However, there are also some grains that only have some of these structures on top. The 150°C sample exhibits more and significantly larger holes continuing along the grain boundaries as well as a significantly larger grain size. Despite this, both large and small grains are still discernible in the BSE image. Furthermore, there are small particles within the holes of the film. In the SE image small spherical structures are present as well, but they are smaller compared to the 100°C sample. The spherical structures seem to be more ordered and they cover most grains entirely. The grain structure of the Au film deposited at 200°C looks similar to the one deposited at 150°C. The elongated holes along the grain boundaries are more extensive leading to less surface coverage of the thin film. The grain size of the larger grains is similar but there are fewer small grains visible in the BSE image. At 250 °C, the Au film becomes fragmented into distinct regions separated by elongated holes along the grain boundaries encompassing multiple grains. The average grain size increases compared to the 200 °C sample. Numerous particles are observed within the holes, varying in size, with both larger and smaller particles being present.

While the images already give a qualitative impression of increasing feature and grain size with rising temperature, the mean surface feature size is determined more quantitative from the SE images using the line intercept method (Table 1). The large surface features are considered and the holes in the 100°C to 250°C are not excluded. The features size increases from 29 nm to 45 nm at 50°C and up to ~70 nm for the 150°C and 200° sample. Only for 250°C the mean features size of the Au film decreases again to 62 nm.

In Figure 28 b) AFM maps of the Au film deposited at 200° C are compared to SEM images at the same magnification. In the larger field of view measurement in i) the AFM map shows similar sized round grain like structures that look different compared to the SEM image. The size of the features is comparable to the size of some areas of the film separated by holes in the SEM image. However, in ii) with a higher magnification the grain structure and size in the AFM map fits to the SEM image, but the surface features in the SE image are not present in the AFM map. The surface roughness R_q measured in the AFM is 2,5 nm.

Table 1: Mean feature size of Au films on sapphire measured with line intercept method from SE images.

| Deposition | RT | 50°C | 100°C | 150°C | 200°C | 250°C |
|--------------|------|-------|-------|-------|-------|-------|
| Temperature | | | | | | |
| Mean Feature | 28,7 | 45,27 | 52,52 | 66,82 | 70,82 | 62,36 |
| Size (nm) | | | | | | |

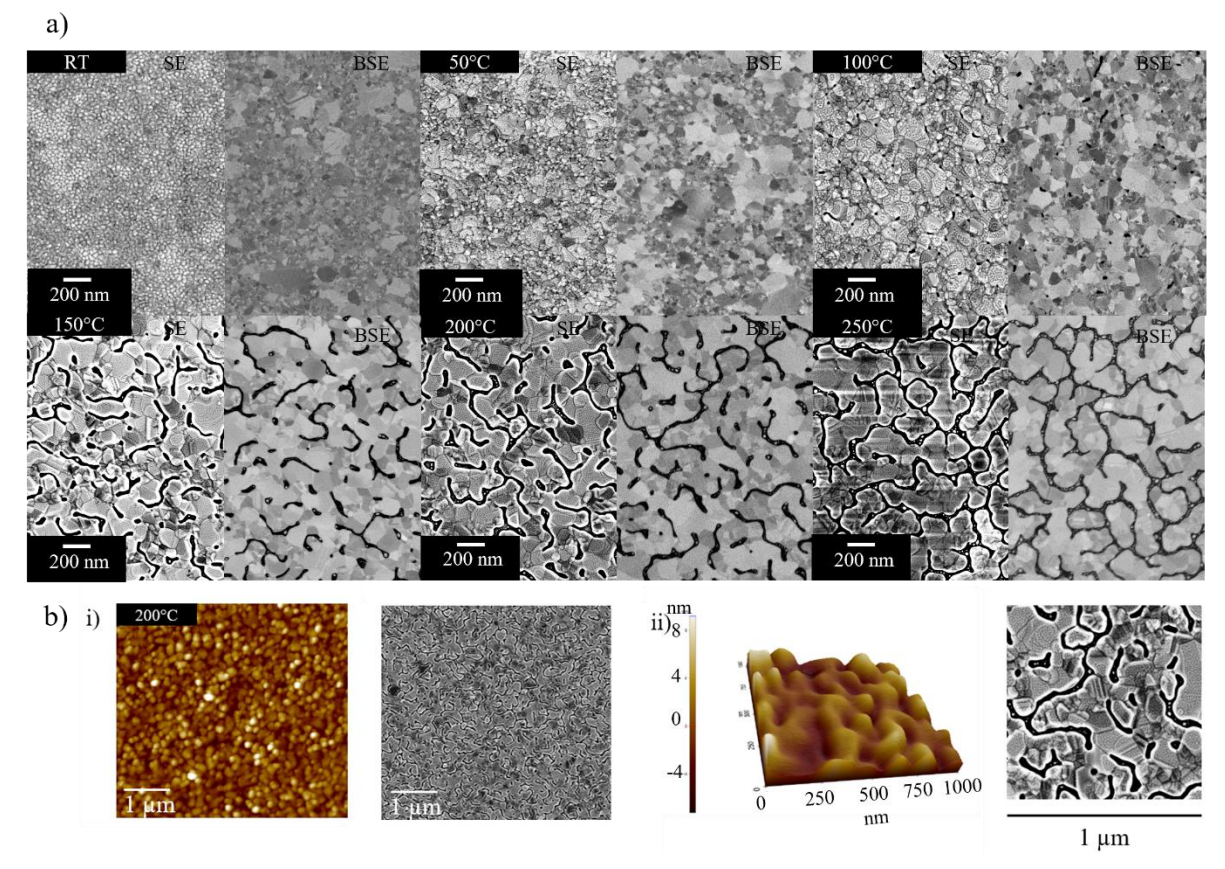


Figure 28: a) SEM images of Au films on sapphire deposited at different temperatures. At low deposition temperatures the film is closed and the grain size is and surface feature size is small. At higher deposition temperature (>100°C) the film is not closed whereby the grain size further increases b) AFM measurements of the Au film deposited at 200°C compared to the SEM images i) low magnification ii) higher magnification and surface roughness; the AFM maps correspond well to the SEM images, but the holes in the film are not tracked precisely.

Texture

In Figure 29 the IPF maps (a) and pole figures (b) of the Au films on sapphire measured via EBSD are presented. In a) the IPF-z maps are at the top and the IPF-x maps at the bottom for each deposition temperature. The grain boundaries are depicted as lines, with boundaries exhibiting a misorientation greater than 10° shown in black, and those with a misorientation less than 10° shown in red. In b) the (111), (110) and (112) pole figures for the RT, 100° C and 250° C sample are shown as well as the (0001), $(10\overline{1}0)$ and $(10\overline{2}0)$ pole figures for the sapphire substrate at the bottom.

Generally, a fibre texture consisting of a strong (111) out of plane texture as well as a random in-plane orientation is present in all samples. The pole figures in b) indicate no significant change of the texture with increasing deposition temperature. Regarding the IPF maps the grain structure looks similar to the BSE images as there are always large and small grains present especially at lower deposition temperatures and there are larger grains at higher temperatures. Additionally, the grain size is determined from the EBSD measurements (Table 2). The grain

size at room temperature is around 40 nm and further increases up to ~80 nm for the 100°C sample. The Au film deposited at 100°C, 150°C and 200°C have a very similar mean grain size in EBSD. However, at 250°C the grain size is noticeably higher with around 150 nm on average.

Table 2: Mean grain diameter of Au on sapphire measured by EBSD.

| Deposition | RT | 50°C | 100°C | 150°C | 200°C | 250°C |
|---------------|-------|-------|-------|-------|-------|-------|
| Temperature | | | | | | |
| Mean Grain | 41,77 | 48,28 | 80,94 | 79,23 | 81,56 | 146,6 |
| Diameter (nm) | | | | | | |

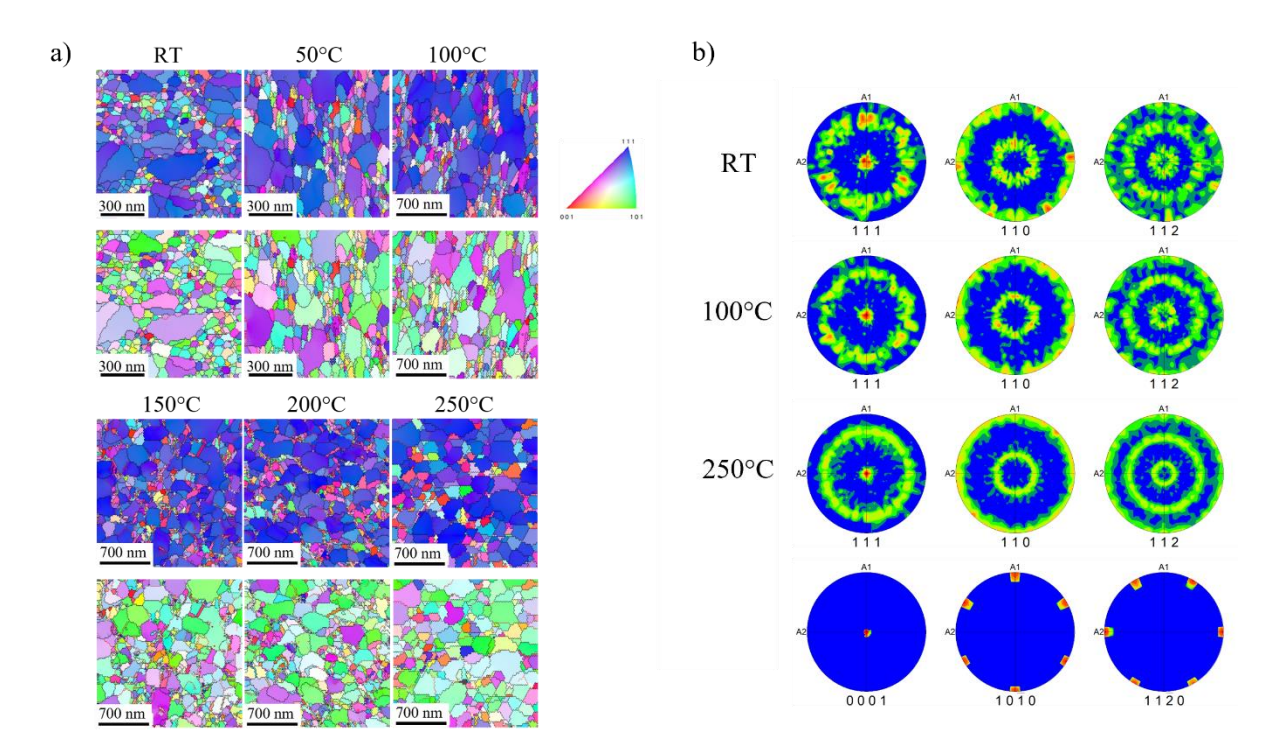


Figure 29: EBSD measurements of Au films on sapphire a) IPF-z maps (top) and IPF-x maps (bottom) b) pole figures of RT, 100° C and 250° C sample and sapphire substrate. The films exhibit a (111) fibre texture and the grain size increases with increasing deposition temperature.

4.1.2 Au on ZnO

Grain structure

For Au on ZnO the measurement series in the SEM, analogous to those for sapphire, is presented in Figure 30 a). At RT deposition of the Au film on ZnO the same microstructure as on sapphire is present. In SE mode grain like topographic features can be observed. The grain structures visible in BSE mode consists of many small grains and some noticeably larger grains. Furthermore, at 50°C the microstructure of Au on ZnO resembles the one of Au on sapphire. The SE image presents larger surface features with some small spherical structures on top as well as smaller surface features that have a similar size to the ones on the RT sample. The grains visible in the BSE image are larger than at RT deposition, but there are large and small grains present. In the SE image of the Au film deposited at 100°C the surface features visible are a little larger to the one observed at 50°C, but there are less smaller features. The larger surface features also have the small spheres on top. Comparing the SE and BSE image, here the surface features resemble the grain structure observable in BSE mode. However, it is noticeable that the grains in the BSE image have a similar contrast, making it hard to distinguish individual grains and already indicating strong in-plane texturing. The 150°C sample exhibits a conspicuous different microstructure. In the SE image large sinuous surface structures separated by grooves and spherical holes are present. Additionally, the film is fully covered by the small spherical structures. Nevertheless, the BSE image indicates that the film is still closed apart from a few small spherical holes. As the contrast between the grains in the BSE image is very low, individual grains cannot be defined by eye. At a deposition temperature of 200°C the microstructure is similar to the 150°C sample. The surface structures are even larger as there are less grooves separating them, but there a many spherical holes. The spherical structures that cover the entire surface of the film look uniformly and ordered. In BSE mode there is even less contrast in the Au film, suggesting an even higher degree of ordering. It can be observed that there are slightly more spherical holes than at a deposition temperature of 150°C. The Au film deposited at 250°C exhibits smaller structures in the SE image compared to the film deposited at 200°C. The grooves are significantly larger and small spherical particles in the grooves can be observed. There are no spherical holes in the film but there are also more grooves. In the BSE image no spherical holes can be observed, but the small particles are visible as they appear to have a dark border around them. In contrast to the 150°C and 200°C sample the grooves in the 250°C sample are also visible in BSE mode as they are a little darker than the Au film. Again, the feature size for each sample is determined from the SE images using the line intercept method (Table 3). The surface structures are measured and the holes are not excluded from the measurement. At room temperature the features have a size of 25 nm. At a deposition temperature of 50°C the features size increases to 46 nm. At 100°C and 150°C the feature size is similar with 63 nm and 66 nm, but it increases up to 103 nm at 200°C. Lastly, for the Au film deposited at 250°C the average feature size decreases again to 96 nm.

Figure 30 a) presents the AFM measurements of the Au film deposited at room temperature (i)) and the Au film deposited at 200° C (ii)) compared to the particular SE image. Comparing both AFM maps to the SEM images the structures observable in the SEM are roughly represented in the AFM maps. The surface roughness R_q in i) is 0,676 nm and in ii) it is 0,541 nm.

Table 3: Mean feature size of Au films on ZnO measured with line intercept method from SE images.

| Deposition | RT | 50°C | 100°C | 150°C | 200°C | 250°C |
|--------------|-------|-------|-------|-------|--------|-------|
| Temperature | | | | | | |
| Mean Feature | 24,52 | 46,02 | 63,35 | 66,28 | 103,17 | 96,45 |
| Size (nm) | | | | | | |

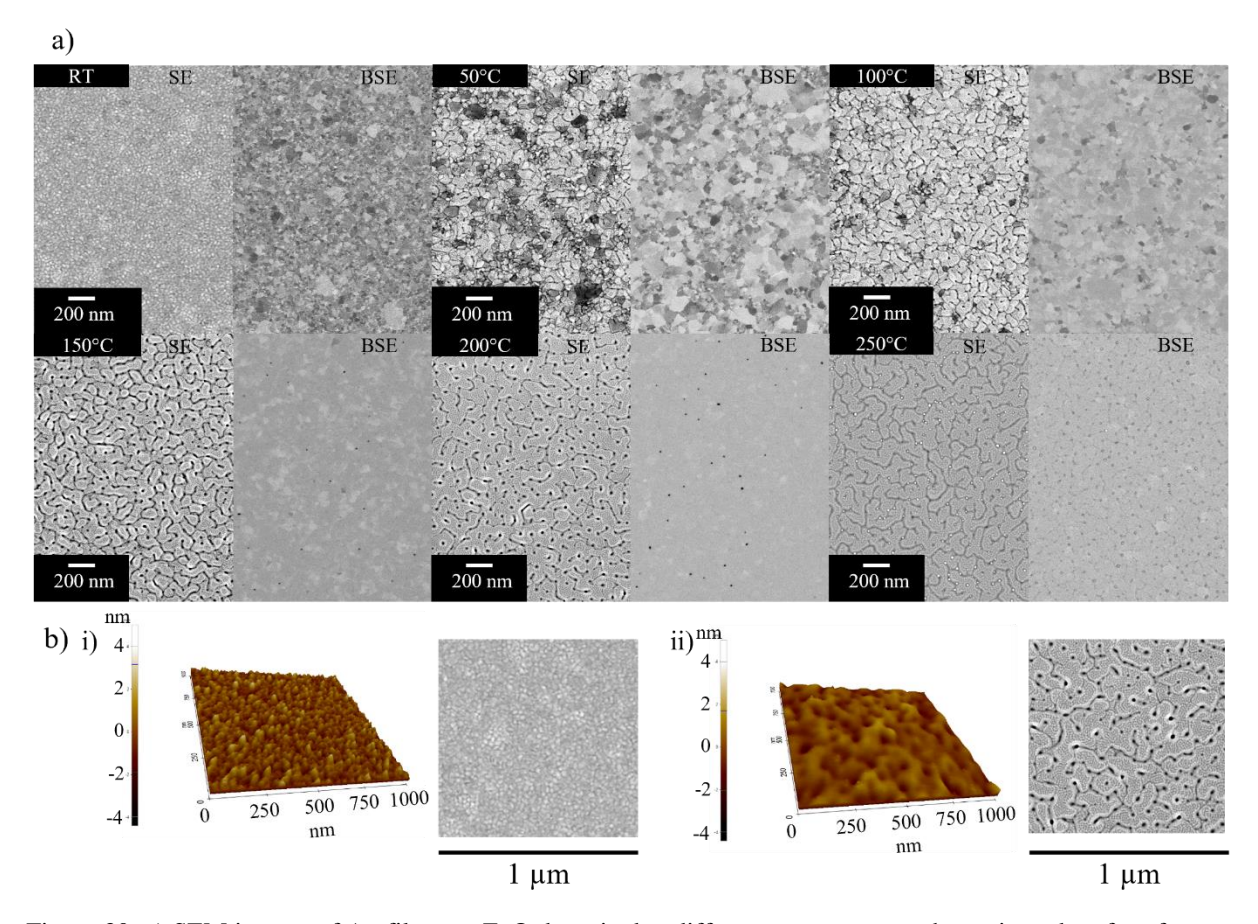


Figure 30: a) SEM images of Au films on ZnO deposited at different temperatures, the grain and surface feature size increase with increasing deposition temperatures; the film is mostly closed, only in the 150°C and 200°C samples small spherical holes are observable b) AFM measurements of the Au film deposited at i) RT and ii) 200°C compared to the SEM images, the surface roughness decreases from RT to 200°C deposition.

Texture

The results of the EBSD measurements are shown in Figure 31. In a) the IPF-z maps (top) and the IPF-x maps (bottom) are shown and the pole figures of the RT, 100°C, 250°C and the ZnO substrate are presented in b).

At RT the pole figures indicate a (111) fibre texture even though the poles seem to be a little off centre. At 50°C the IPF-z shows that a preferred (111) out of plane texture is present, while in the IPF-x map no preferred in plane orientation can be observed. The Au film deposited at 100°C exhibits a clear (111) out of plane orientation, but also a preferred in plan orientation. Most grains show OR2 and some grains with OR1 are present as well. The pole figure confirms the primarily presence of OR2. From 150°C to 250°C the (111) out of plane and OR2 in plane orientations become more and more pronounced, leading to a mazed bicrystal microstructure consisting primarily of OR2, explaining also the similar contrast of all the grains observed in the BSE images. The pole figure of the 250°C has very well-defined poles confirming a clear epitaxial relation. Additionally, the grain boundaries depicted as black lines (misorientation > 10°) of the 150°C, 200°C and 250°C samples are all twin grain boundaries (60° misorientation). The mean grain diameter is also determined using EBSD (Table 4). The grains sizes of the RT and 50°C sample are similar with 52 nm and 53 nm. At 100°C the grain size increases up to 94 nm and then further to 166 nm at 150°C. From 150°C to 200°C the grains become significantly larger as the grain diameter at 200°C is 505 nm. For the Au film deposited at 250°C the grain diameter decreases to 379 nm.

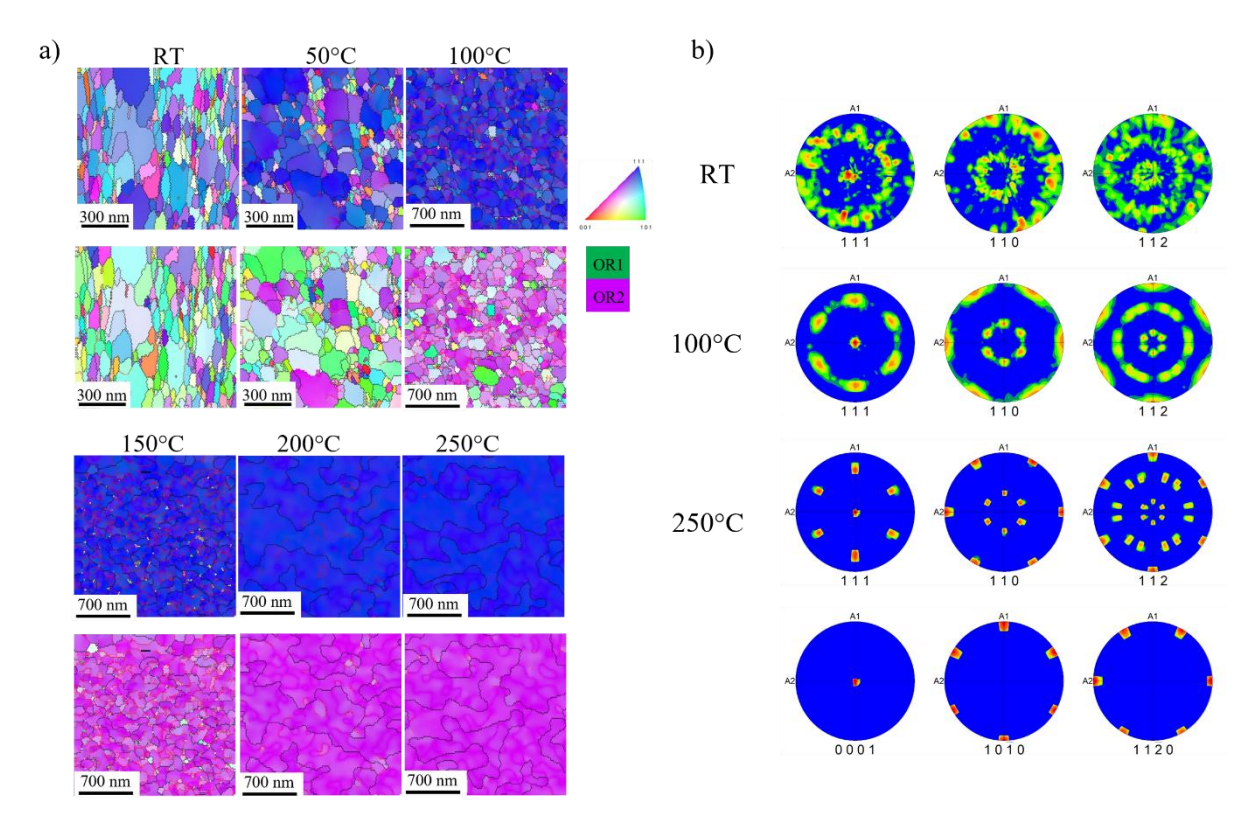


Figure 31: EBSD measurements of Au films on ZnO a) IPF-z maps (top) and IPF-x maps (bottom) b) pole figures of RT, 100° C and 250° C sample and ZnO substrate. The RT and 50° C samples have (111) fibre texture, but from a deposition temperature of 100° C a preferred in plane orientation (OR2) can be observed. The grain size increases significantly at deposition temperatures of 150° C and above.

Table 4: Mean grain diameter of Au on ZnO measured by EBSD.

| Deposition | RT | 50°C | 100°C | 150°C | 200°C | 250°C |
|---------------|-------|-------|-------|-------|-------|-------|
| Temperature | | | | | | |
| Mean Grain | 53,15 | 52,14 | 93,95 | 165,8 | 505,1 | 378,5 |
| Diameter (nm) | | | | | | |

4.2 Microstructure evolution at 800°C

In this study, not only the influence of the substrate temperature during thin film deposition on the Au film's microstructure is investigated, but also its effect on the microstructural evolution during subsequent post-annealing at 800°C in the RTA. The following section presents the results concerning the microstructural development at 800°C.

4.2.1 Au on sapphire

Film Morphology

Figure 32 presents the SEM images of the post-annealed Au films on sapphire substrates. All images are taken in BSE mode.

At 800 °C, the 40 nm Au film on sapphire undergoes SSD, evolving into discrete particles. A clear influence of the initial deposition temperature on the resulting microstructure is observed, with particle size decreasing as the deposition temperature increases (Figure 32). Additionally, the particle density increases (c.f. Table 5).

The film deposited at room temperature evolves into large, elongated islands, with smaller particles located between them. The mean particle size is 5.26 µm. For the film deposited at 50 °C, the overall morphology is similar; however, the elongated structures are thinner, resulting in a reduced mean particle size of 1.33 µm. At 100 °C, the microstructure changes significantly. The particles are smaller and more uniform, with a mean size of 520 nm. While some elongated features persist, most particles exhibit a more rounded and faceted morphology. The morphology of the particles on the sample deposited at 150 °C resembles that of the 100 °C sample, though the mean particle size further decreases to 320 nm. A broader size distribution is observed, with both smaller and larger particles present. The particles are uniformly faceted and typically round or slightly elongated in shape. This trend continues for the sample deposited at 200 °C, where the mean particle size decreases slightly to 210 nm.

In contrast, the Au film deposited at 250 °C exhibits a markedly different particle morphology and size distribution. The particles are significantly smaller, with a mean size of 70 nm. They are generally not faceted and consist of a mixture of small, rounded particles and larger, irregularly shaped particles.

Table 5: Mean particle size of Au on sapphire after post annealing dependent on the deposition temperature.

| Deposition | RT | 50°C | 100°C | 150°C | 200°C | 250°C |
|------------------|------|------|-------|-------|-------|-------|
| Temperature | | | | | | |
| Mean Particle | 5,26 | 1,33 | 0,52 | 0,32 | 0,21 | 0,07 |
| Size (µm) | | | | | | |
| Particle Density | 0,19 | 0,75 | 1,91 | 3,04 | 4,72 | 13,74 |
| (μm^{-1}) | | | | | | |

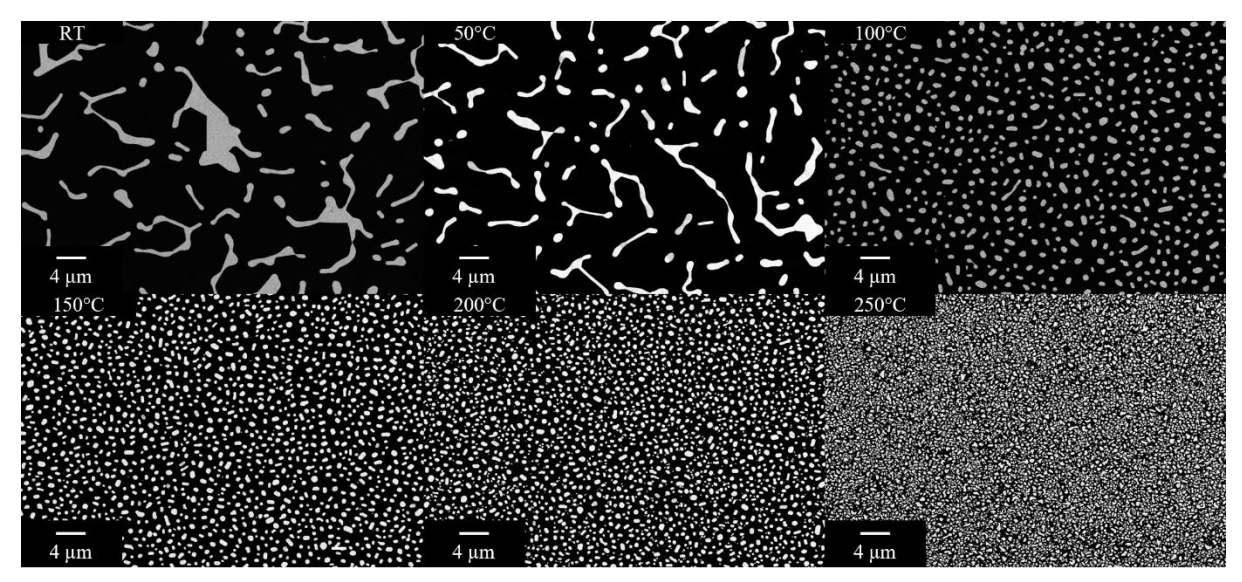


Figure 32: SEM images of Au films on sapphire deposited at different temperatures and post-annealed at 800°C for 5 minutes. All films evolved into particles; the particle size decreases with increasing deposition temperature.

Texture

The results of the EBSD measurements are shown in Figure 33, where a) are the IPF maps and b) the pole figures of the RT, 100°C and 250°C samples as well as the sapphire substrate at the bottom. It is noticeable that the texture of the particles is not dependent on the initial deposition temperature of the film. All particles express a (111) fibre texture. In the IPF maps it is visible that many data point are excluded from the evaluation due to a very low confidence index of the measurement, located at the side facets of the particles. The number of excluded data points increases with decreasing particle size due to the topography.

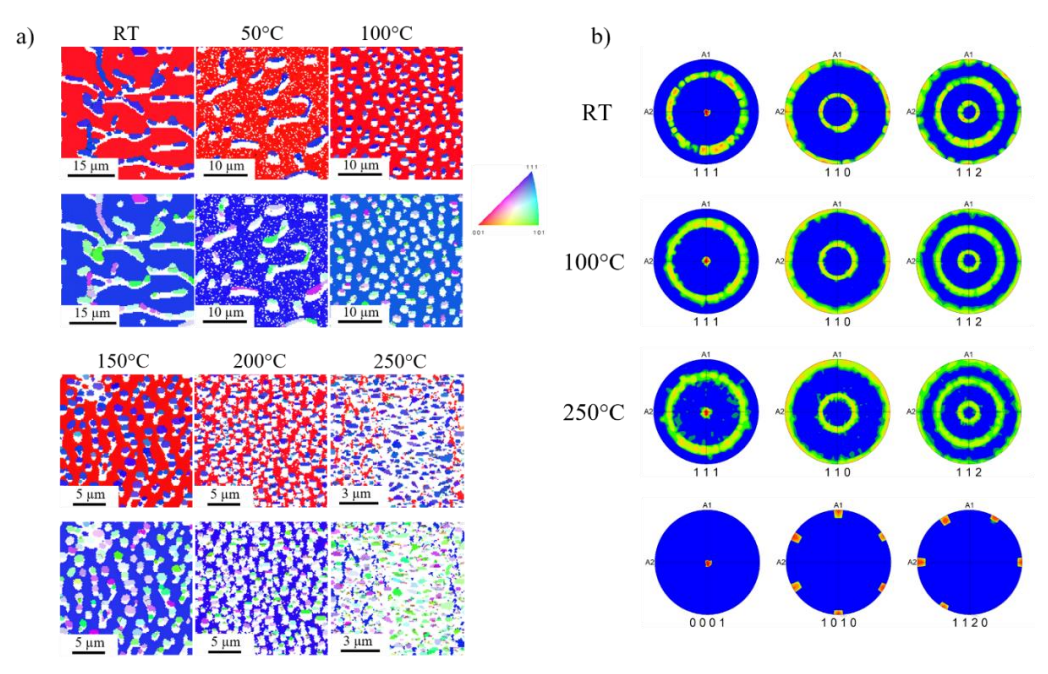


Figure 33: EBSD measurements of Au films on sapphire after post-annealing at 800°C a) IPF-z maps (top) and IPF-x maps (bottom) b) pole figures of RT, 100°C and 250°C sample and sapphire substrate. All particles have a (111) fibre texture.

4.2.2 Au on ZnO

Film Morphology

The SEM images of the post-annealed Au on ZnO samples are presented in Figure 34. These images are taken in SE mode.

The samples deposited at RT and 50 °C exhibit elongated particles. The post-annealed film deposited at 50 °C has a mean particle size of 1.4 µm, whereas the RT-deposited film has a smaller mean particle size of 0.5 µm. For the sample deposited at 100 °C, the film undergoes partial dewetting, forming interconnected elongated structures, while large continuous islands remain. These islands display hole formation primarily along their edges, and only a few fully separated particles are present. The sample deposited at 150 °C is nearly continuous, featuring both large and small holes across its surface. Similarly, the 200 °C sample exhibits a closed film, albeit with a greater number of holes. However, these holes are more uniformly sized and slightly smaller than those observed in the 150 °C sample. At a deposition temperature of 250 °C, the film also appears nearly continuous, with significantly fewer and smaller holes compared to the 200 °C sample. Additionally, rounded agglomerates of gold are observed on top of the film surface. These agglomerates are uniformly distributed across the substrate.

The qualitative impressions gained by SE imaging was further quantified by segmenting the images and extracting the covered area. The surface coverage of the gold film is 21% for the RT sample and slightly decreases to 18% for the 50 °C sample. As the film becomes progressively more continuous from 100 °C to 250 °C, the covered area increases correspondingly. The highest coverage is achieved for the 250 °C sample, with a surface coverage of 99.2%.

Table 6: Mean particle size and covered area of Au on ZnO after post annealing dependent on the deposition temperature.

| Deposition | RT | 50°C | 100°C | 150°C | 200°C | 250°C |
|---------------|------|-------|-------|-------|-------|-------|
| Temperature | | | | | | |
| Mean Particle | 0,50 | 1,40 | - | - | - | - |
| Size (µm) | | | | | | |
| Covered Area | 21,0 | 18,07 | 46,48 | 95,96 | 95,66 | 99,20 |
| (%) | | | | | | |

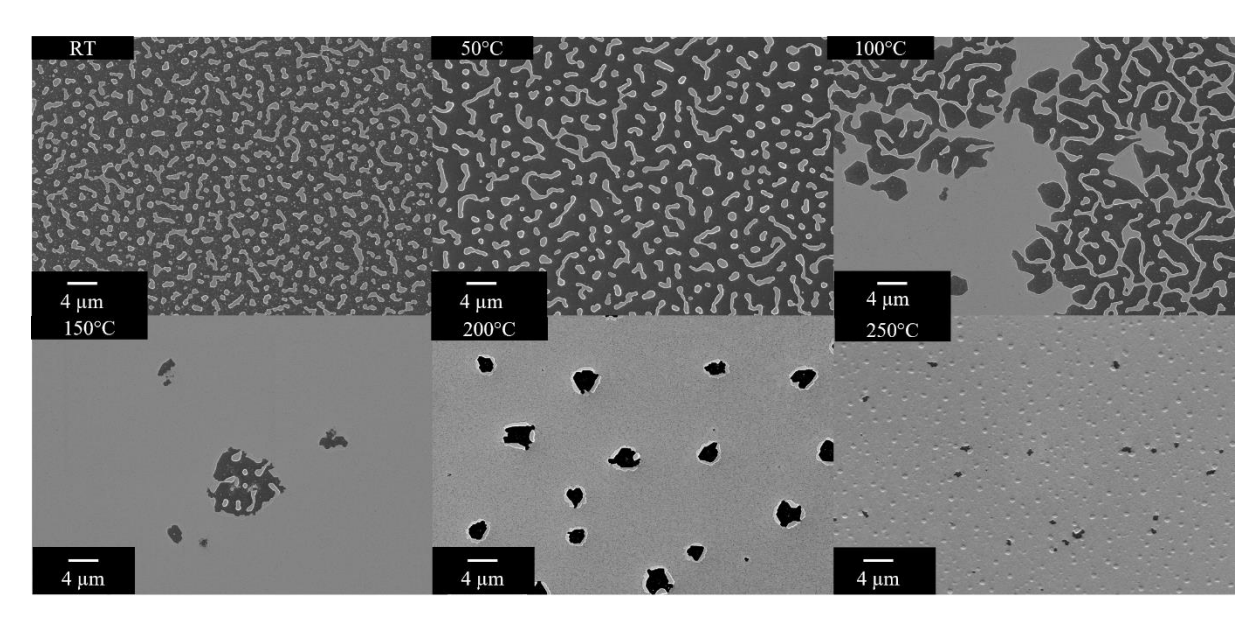


Figure 34: SEM images of Au films on ZnO deposited at different temperatures and post-annealed at 800°C for 5 minutes. The films deposited at RT and 50°C evolve into particles, at 100°C closed islands and dewetted areas are present while at higher deposition temperatures the films remain closed with some holes. Additionally, on the 250°C sample hillocks can be observed on the surface of the film.

Texture

Figure 35 presents the EBSD measurements of the post-annealed Au on ZnO samples. In a) the IPF maps are shown and in b) the pole figures of the RT, 100°C and 250°C and the ZnO substrate are presented. All samples exhibit a preferred (111) out of plane orientation. The particles on the RT and 50°C are not epitaxial even though OR2 is already slightly preferred which can be observed in the pole figures especially. The 100°C sample exhibits epitaxy, but has both OR1 and OR2. The large, closed island is OR1 whereas the dewetted fingers are OR2. The 150°C to 250°C samples that have a nearly closed film only show OR2. Furthermore, these samples exhibit twin grain boundaries only.

Additionally, the mean grain diameter of the samples with a closed film (150° to 250°C) is also determined by EBSD. The 150°C and 200°C sample both have grain diameter of 2,3 μ m and the 250°C sample has a grain diameter of 1,88 μ m.

Table 7: Mean grain diameter of Au on ZnO after post-annealing measured by EBSD.

| Deposition | RT | 50°C | 100°C | 150°C | 200°C | 250°C |
|---------------|----|------|-------|-------|-------|-------|
| Temperature | | | | | | |
| Mean Grain | - | - | - | 2,30 | 2,30 | 1,88 |
| Diameter (µm) | | | | | | |

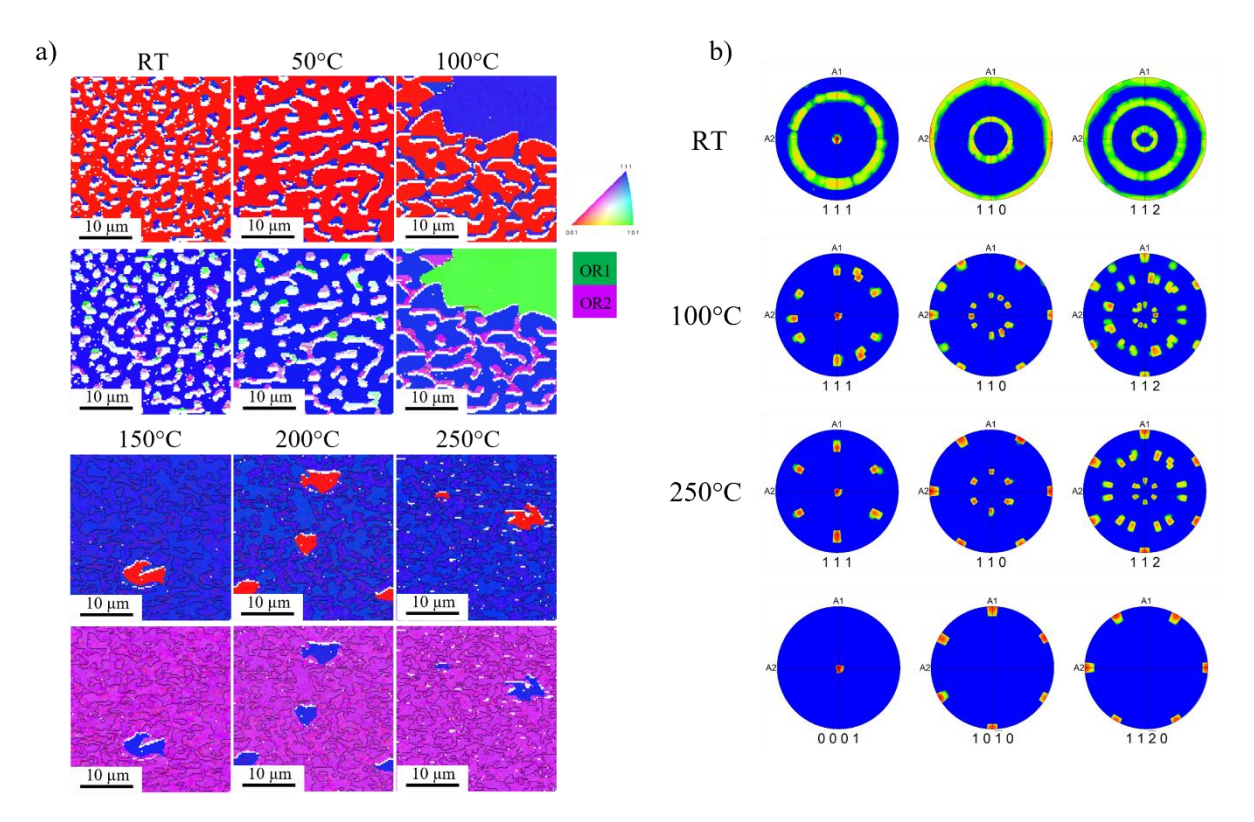


Figure 35: EBSD measurements of Au films on ZnO after post-annealing at 800° C a) IPF-z maps (top) and IPF-x maps (bottom) b) pole figures of RT, 100° C and 250° C sample and ZnO substrate. The particles have a (111) fibre texture, the 100° C sample has closed islands with OR1 and dewetted areas with OR2. The films deposited at 150° C and higher temperatures exhibit OR2 only as well as very large grains.

5 Discussion

In this section the results presented in chapter 4 will be evaluated and discussed.

5.1 Temperature control during E-beam deposition

This work focuses on the influence of temperature during deposition in the E-beam. Therefore, it is essential to first consider how precisely the temperature can be controlled. In an ideal experiment, the temperature would remain perfectly constant and could be measured directly at the substrate surface. However, in the setup used here, this is unfortunately not feasible, which means that several additional factors must be taken into account.

In these experiments, the temperature is not constant during deposition, but it does not deviate more than 10 °C from the target temperature. The thermocouple used to measure the temperature is placed underneath the substrate holder and the heater is located above the substrate holder.

It is reported in several studies about evaporation at elevated temperatures that the measured temperature at the thermocouple deviates from reality. Levlin et al. measured temperature differences between the sides of the substrate of up to 75 K which demonstrates that the location of the heater and the thermocouple relative to the substrate surface needs to be considered [5]. In another study, Belous et al. come to a similar conclusion as they mention that the temperature the thermocouple measured provides an approximate impression only. Looking at the temperature of the thin film during deposition it is observable that the film temperature scales with the substrate temperature but is with about 400 K -500 K considerably higher [6].

5.2 Influence of temperature during E-beam deposition of thin Au films

As presented in chapter 4 Result, the substrate temperature plays a crucial role in determining the growth behaviour and microstructure of Au thin films on metal oxide substrates. The following section analyses the resulting microstructure in relation to the substrate material and deposition temperature.

One of the key findings is that both grain size and surface feature size increase with increasing substrate temperature. This trend is illustrated in Figure 36, where a) and b) display the grain and surface feature sizes of Au deposited on sapphire, while c) and d) show the same for Au on ZnO. Surface features are evaluated from SE images, whereas grain size is determined via EBSD, as described in chapter 4.1.1 Au on sapphire and chapter 4.1.2 Au on ZnO.

Grain growth at higher temperatures is expected, as both the initial grain size at impingement and subsequent grain growth are temperature-dependent processes. At elevated temperatures, the increased mobility and energy of incoming adatoms raise the critical cluster size for nucleation while decreasing the nucleation rate. This leads to the formation of fewer but larger nuclei in the early growth stages, resulting in a larger grain size at impingement. Additionally, grain growth in later stages, driven by grain boundary and surface self-diffusion, is also enhanced at higher temperatures, further promoting grain coarsening [2].

At room temperature and 50 °C, the microstructure of Au films on sapphire and ZnO is relatively similar. However, with increasing substrate temperature, substrate-specific effects become more pronounced. For instance, at 250 °C, the grain size of Au on sapphire reaches approximately 140 nm, which aligns with the empirical observation that, in normal grain growth, the grain size typically does not exceed three times the film thickness (here, ~40 nm) [2]. In contrast, the grain size of Au on ZnO at 200 °C reaches ~500 nm, indicative of abnormal grain growth, a phenomenon also reported in literature by Dierner et al. [35] for Au on ZnO systems after post-annealing. From 150 °C, the Au films on ZnO exhibit clear epitaxial growth, accompanied by a more uniform and significantly larger grain size. This suggests a strong substrate influence, where the epitaxial relationship promotes abnormal grain growth, consistent with reports of similar behaviour after post-deposition annealing [35].

The grain size distribution for Au on sapphire consistently shows a bimodal character. At higher deposition temperatures, the population of larger grains increases, while smaller grains progressively disappear. This behaviour can be attributed to energetic considerations as reducing grain boundary area minimizes the total system energy [2]. Additionally, grains with favourable orientations grow at the expense of less favourable ones to lower the surface energy of the film [2], a process accelerated by enhanced atomic mobility at elevated temperatures. At lower temperatures, limited atomic mobility slows this coarsening process, resulting in a greater number of small grains [2].

For Au films on sapphire, a comparison of grain size and surface features reveals a discrepancy at RT, where surface morphology does not reflect the underlying grain structure. In contrast, at elevated deposition temperatures, the visible grooves and steps in SE images correspond well with grain boundaries. For Au on ZnO, surface topography reflects the grain structure only at 50 °C and 100 °C. At higher temperatures, the grain size exceeds the scale of surface features, indicating that the observed structures in SE images represent topography rather than grains. However, since grain size and feature size are obtained through different methods and surface features include holes the values are not directly comparable, and surface feature size is likely underestimated.

The second key finding is that films deposited at elevated temperatures are not fully closed, as shown in Figure 36 e), suggesting that the critical thickness required for continuous film formation increases with temperature. This effect is distinct in the Au films on sapphire. While the average grain size of Au on sapphire is similar at $100\,^{\circ}\text{C}$ and $150\,^{\circ}\text{C}$ (Figure 36 c), the overall film coverage decreases significantly with increasing temperature (Figure 36 e). Voids form along grain boundaries and grow with temperature, indicating that the critical thickness exceeds 40 nm beyond $100\,^{\circ}\text{C}$. This is consistent with a reduced nucleation density at higher temperatures, which is commonly observed due to increased adatom mobility. A smaller number of islands and potentially a reduced δ -zone at higher temperatures means that more material is required to achieve film closure [2], [16]. As a result, some islands fail to impinge, leaving voids, especially at grain boundaries. At $200\,^{\circ}\text{C}$ and $250\,^{\circ}\text{C}$, these voids become larger, and at $250\,^{\circ}\text{C}$, isolated islands are present.

In the case of ZnO, Au films deposited at 150 °C and 200 °C are also not fully closed, as depicted in Figure 36 b). However, in contrast to the sapphire samples, the holes are small and spherical and are not clearly discernible located along grain boundaries, indicating a different growth mechanism. Notably, the Au film on ZnO appears more continuous at 250 °C, lacking the clear holes seen at lower temperatures, instead, spherical particles are observed. Nevertheless, SE images reveal significantly wider and deeper surface grooves, which are even faintly visible in BSE images, suggesting a more pronounced topographical variation.

The observation that Au films exhibit a lower covered area on sapphire compared to ZnO at elevated deposition temperatures, and consequently a higher critical thickness, can be well explained by comparing the texture of the Au films on both substrates. Figure 37 a) and b) compare the (111) pole figures of Au films deposited at room temperature (top), 250 °C (middle), and the respective substrates (bottom) for sapphire and ZnO. As noted earlier, the Au films on ZnO exhibit an epitaxial relation at elevated temperatures leading to abnormal grain growth which stabilizes the film compared to the Au films on sapphire. According to literature, two orientation relationships (ORs) are typically observed for Au on ZnO: OR1 and OR2. Jedrecy et al. [47] found for Ag on ZnO (similar fcc structure to Au) that OR2 is geometrically favoured due to the alignment of densely-packed atomic rows. This alignment reduces lattice

mismatch strain through the formation of a long-range coincidence lattice, typically with a periodic match every 8 ZnO and 9 Ag unit cells. OR2 also places metal atoms directly over Zn rows, which is energetically more favourable than the bridge-like positions found in the rotated OR1 orientation. As a result, OR2 minimizes interfacial energy and promotes the growth of relaxed, well-ordered islands, making it the geometrically preferred epitaxial orientation. Dierner et al. [35] observed for Au on ZnO that at lower temperatures, OR2 is favoured, while OR1 tends to dominate after post-annealing at 800 °C. Here, at 100 °C, OR2 is already the predominant orientation, although a small fraction of grains still adopts OR1. From 150 °C onward, only OR2 is observed.

Additionally, at 100 °C, the grains are relatively small, and high-angle grain boundaries dominate. At higher substrate temperatures, the grains become significantly larger and are primarily separated by twin or low-angle grain boundaries, both of which are energetically more favourable [2], [48]. Hence, the development of a pronounced crystallographic texture can reduce the total energy of the film by minimizing surface, interfacial and grain boundary energies [2]. On ZnO substrates, this effect contributes to enhanced thermal stability and a reduced critical thickness at elevated temperatures compared to sapphire. This suggests that textured, epitaxial growth supports earlier film closure, even in the presence of increased adatom mobility.

On sapphire a (111) fibre texture is observed. However, the out-of-plane (111) orientation becomes increasingly pronounced with higher substrate temperatures. This is further illustrated in Figure 37 c), which shows the pseudo-rocking curves of the (111) pole figures for Au on sapphire. From room temperature to 100 °C, the peak intensity increases and the peak width narrows, indicating an increasingly well-defined texture. Between 100 °C and 250 °C, however, the intensity decreases and the peak broadens, likely due to the presence of voids in the film, which influence the measurement. Despite this, the (111) fibre texture becomes generally stronger with increasing deposition temperature, lowering the total energy of the film.

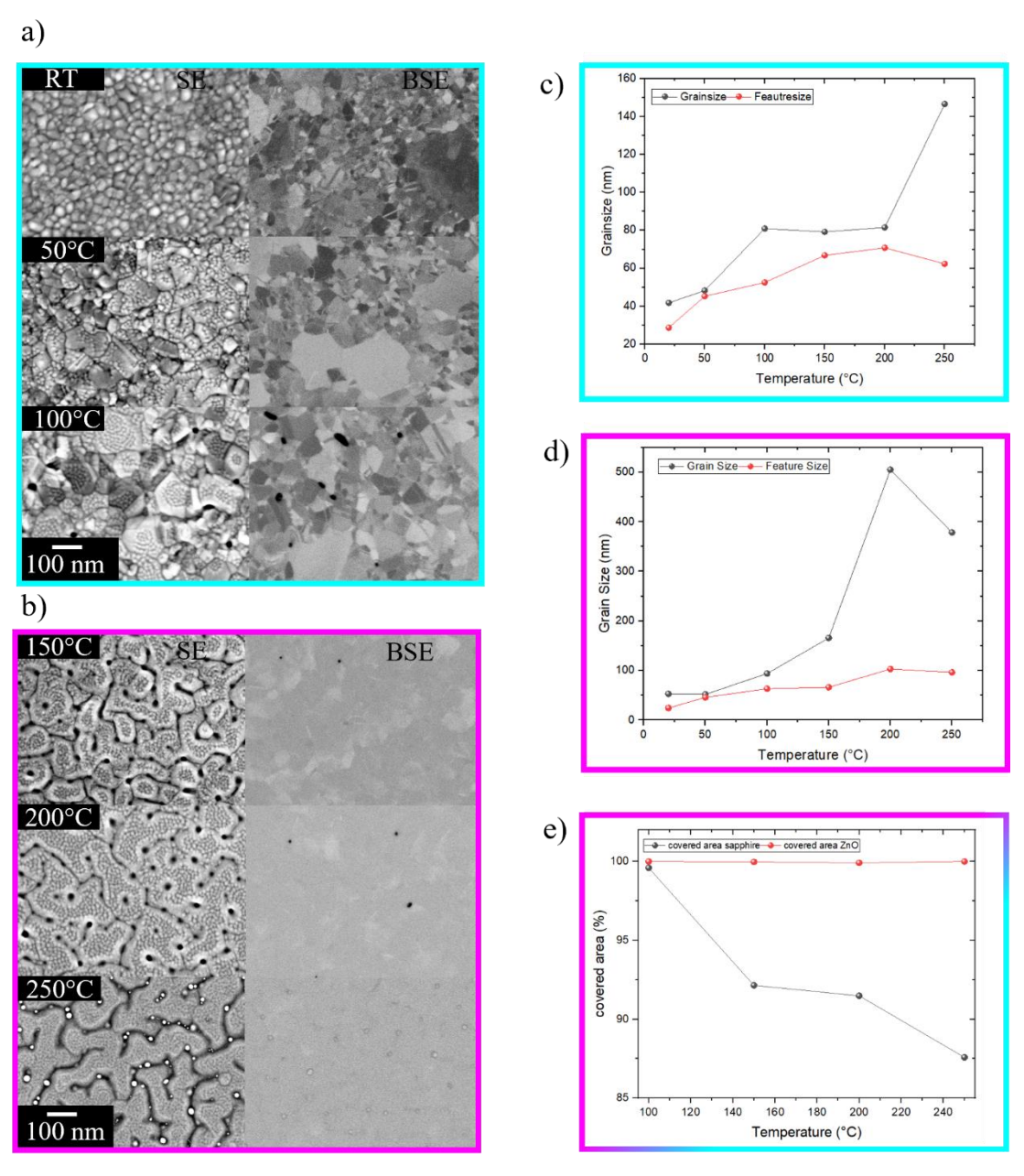


Figure 36: Grain size and features size of Au on sapphire (cyan) (a), c)), the grain and feature size increases with due to increases grain growth at higher temperatures; grain size and surface feature size of Au on ZnO (magenta) (b), d)), strong increase in grain size, indicating abnormal grain growth at higher deposition temperatures due to epitaxial growth of the film, feature size increases, but is a lot smaller than grain size; covered area of as-dep films e), Au films on ZnO remain mostly closed whereas covered area of Au on sapphire decreases, indicating a lower critical thickness of Au on ZnO at elevated temperatures that also correlates with the epitaxial growth of the films.

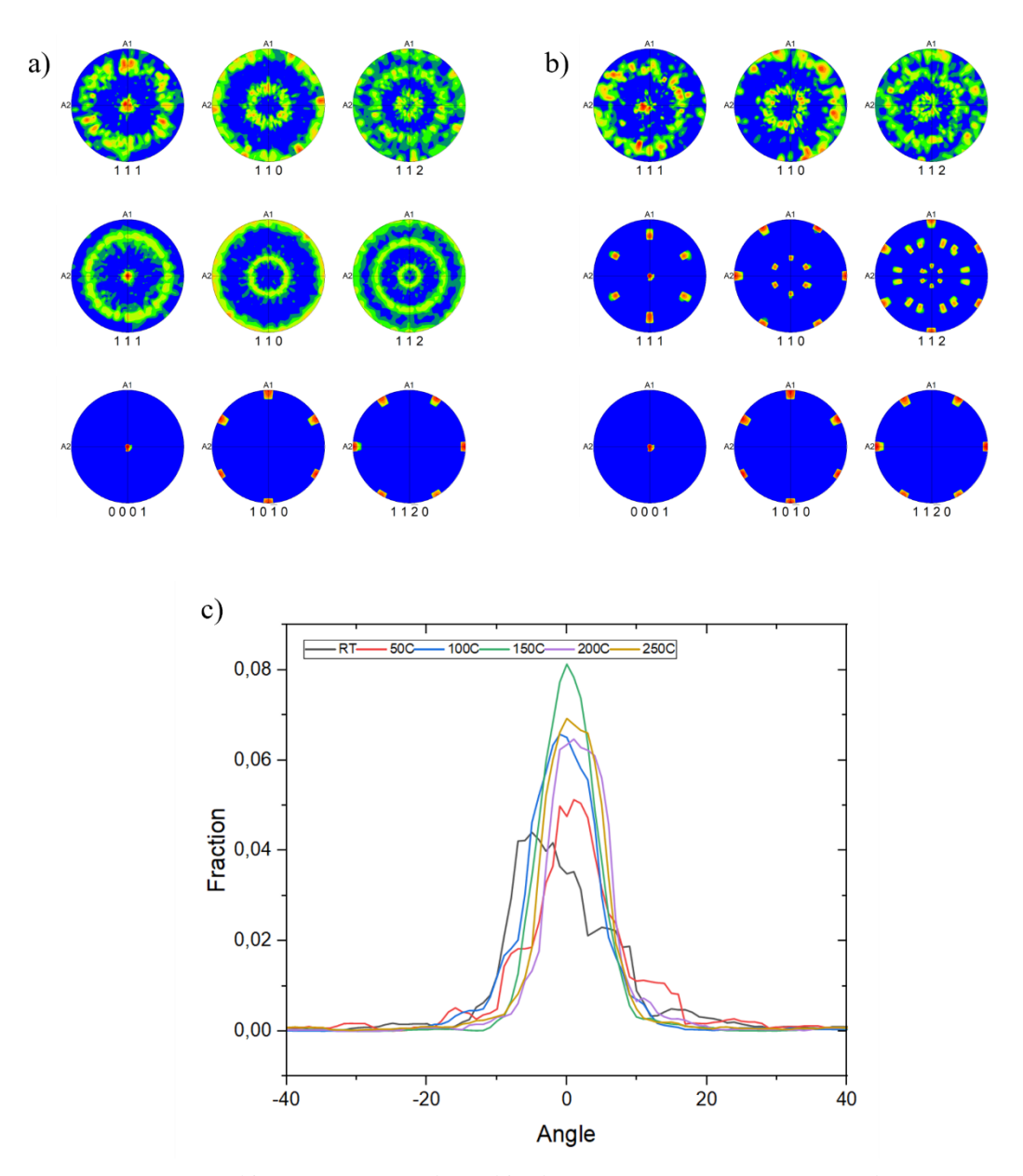


Figure 37: a) PF Au on sapphire RT, 250°C and sapphire b) PF Au on ZnO RT, 250°C; the texture at RT is similar, but at elevated temperatures the influence of the substrate becomes more dominant as on ZnO the films grow with a preferred in-plane orientation (OR2) c) pseudo rocking curves of (111) PF of Au on sapphire, a (111) fibre texture is present in all samples, but the peak sharpens since the fibre texture becomes more pronounced with increasing deposition temperatures.

Thin film growth at elevated temperatures

To gain deeper insight into the growth behaviour of Au on ZnO, cross-sectional lamellas of samples deposited at RT and 200 °C were examined using STEM. Figure 38 a) shows the cross-section of the Au film deposited at RT, while Figure 38 b) presents the film grown at 200 °C. The RT-deposited film exhibits an average thickness of 38 nm, closely matching the intended 40 nm. In the magnified region to the right, grain boundaries are traced in red. The grains

exhibit a non-columnar morphology, instead resembling the so-called Type 1 thickening described in literature [2]. This growth type is characterized by immobile grain boundaries and limited coarsening after film coalescence. These observations are consistent with the expectations from zone models: at low homologous temperatures (zone 1), limited adatom mobility and strong shadowing effects dominate growth, resulting in a grain structure that largely reflects the initial nuclei. Although energetically favourable grains may grow preferentially, the restricted grain boundary mobility hinders the elimination of less favourable orientations consistent with the EBSD measurements presented in Figure 37. Consequently, the film exhibits irregular grain boundaries and high surface roughness [13], [18]. This increased roughness is confirmed by SE imaging and AFM measurements for the RT film. In contrast, the film deposited at 200 °C (Figure 38 b)) exhibits a distinctly different microstructure. It appears highly uniform, with no clearly resolved grain boundaries. Due to the channelling contrast in BSE mode grains with similar orientations appear in a similar shade [37]. Unlike sapphire, all grains have a similar orientation (OR2), so they cannot be distinguished from the BSE images. The film thickness remains 38 nm, indicating that deposition temperature does not influence the final thickness under these conditions. Surface grooves observed in SE images are also visible in the cross-section and do not fully penetrate the film, they reach a depth of approximately 10 nm. Aside from these grooves, the surface appears flat, in agreement with the AFM results, which show a reduced roughness compared to the RT sample. However, the AFM measurements do not resolve smaller features or detect the holes visible in SE images. This limitation is attributed to the AFM tip geometry since the cantilever tip has a diameter of 16 nm, while the holes observed have diameters of approximately 20 nm, and many grooves and features are below 10 nm in width, thus, below the resolution limit of the tip.

The uniform grain structure, reduced surface roughness, and significantly larger grain size all suggest that film growth at 200 °C corresponds to zone 2 in the structure zone model. In this regime, surface diffusion becomes the dominant mechanism, promoting grain growth through surface recrystallization and leading to the development of a columnar structure [13], [18]. The small spherical structures observed at elevated temperatures may be recrystallized islands forming on the grain surfaces. Their increasing regularity with temperature supports this hypothesis.

Given that the 150 °C sample exhibits similar characteristics to the 200 °C film, a progression of growth regimes can be proposed: RT growth corresponds to zone 1, 50 °C and 100 °C represent a transitional regime (with limited recrystallization and some enhanced grain growth), and from 150 °C onward, growth clearly aligns with zone 2 characteristics.

An additional feature of the 200 °C lamella is a void with an hourglass shape, featuring a small Au particle at the interface. This may explain why some spherical holes seen in SE images are not visible in BSE imaging. When the hole narrows and retains Au at the interface, it may not be detected in standard SEM modes. Interestingly, voids are consistently found beneath surface

grooves. Some contain small agglomerates of material, similar to the particles observed in the 250 °C sample, where larger grooves and distinct surface particles are clearly visible. Such particles are also present in the 200 °C sample but are mostly covered by the continuous Au film. The consistent positioning of voids beneath grooves suggests a distinct closure mechanism. Unlike on sapphire, closure on ZnO may initiate near the middle of the film. This would leave grooves at both the surface and the interface. It is conceivable that surface features originally correspond to discrete islands that first coalesce centrally. Due to the epitaxial relation with the substrate, which imposes both in-plane and out-of-plane orientation, grain boundaries might not necessarily persist after island impingement.

However, this hypothesis does not fully explain the absence of holes in the BSE image of the 250 °C sample, whereas such holes are clearly present at 150 °C and 200 °C.

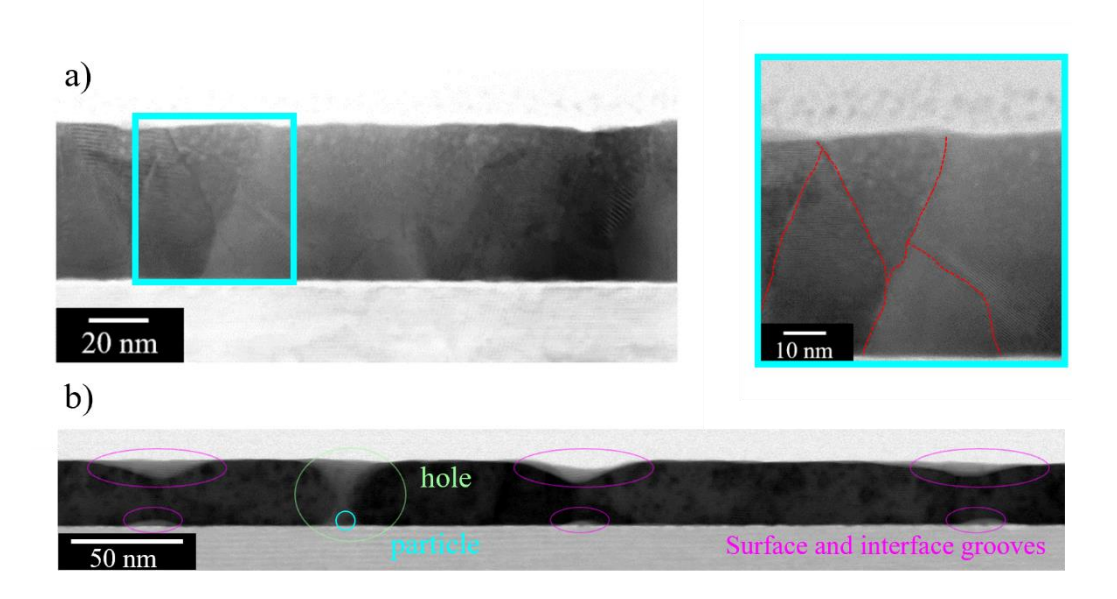


Figure 38: STEM images of cross section lamellas of Au on ZnO deposited at a) BF images of RT with cut-out where grain boundaries are marked in red; the grains do not grow columnar but exhibit a grain structure similar to type 1 growth b) DF image of 200°C with surface and interface grooves marked in purple and hole marked in green, an hourglass shaped hole with a particle in the middle can be observed as well as hols at the interface of the film. The surface grooves are located above the holes at the interface indicating that the film closed at first in the middle of their thickness.

5.3 Effect of post-annealing at 800°C on the microstructure of thin Au films

Since the substrate temperature during deposition effects the microstructure of the thin film, the microstructural evolution at 800°C is also influenced by the initial deposition temperature. In the following sections the microstructure exhibited after post-annealing will be discussed with reference to the as-deposited microstructure.

5.3.1 Au on sapphire

Figure 39 a) and b) present the data from 4.2.1 Au on sapphire. In a) the particle size is compared to the particle density whereas in b) the particle size is compared to the initial grain size of the as-deposited Au films.

It is clearly visible that with increasing initial grain size of the as-deposited film the particle size decreases constantly whereas the particle density increases. This finding disagrees with the literature where Haustrup et al. [12] found that the particle size increases with increasing initial grain size. However, in literature it is assumed that the film is closed. Here, the covered area of the film decreases with increasing substrate temperature which affects the dewetting process. The films deposited at 100°C, 150°C and 200°C have similar initial grain sizes, but the covered area of the as-deposited samples decreases noticeably (Figure 36 e)). However, the decreasing covered area corresponds with the decreasing particle size. In Figure 39 c) a BSE image of the Au film deposited at 250°C (left) and the corresponding sample after postannealing imaged in SE mode at the same magnification (right) are shown. As described before, the as-deposited film is still separated into islands leading to a further decrease in covered area whereas the initial grain size increases (Figure 36 c) and e)). Comparing the isolated areas of the as-deposited film with the particles it is conspicuous that the size and shape is similar. Therefore, it leads to the assumption that the particles directly form from the separated areas in the as-deposited film as the film retracts and the pre-existing voids expand at 800°C. Since the decreasing covered area corresponds with the decreasing particle size, it indicates that the dominant factor for the particle size is not the initial grain size, but the pre-existing voids in the as-deposited films.

Additionally, it must be considered that multiple competing processes occur at elevated temperatures. On one hand, grain growth takes place, which minimizes the grain boundary energy [2]. In this context, grains with a more energetically favourable orientation ((111) fibre texture for Au on sapphire) tend to grow at the expense of less favourably oriented grains, leading to their elimination [2], [31]. On the other hand, surface and interface energy minimization of the film occurs via SSD, where grain boundaries or pre-existing voids act as initiation sites [8]. Consequently, in the RT as-deposited films, it is likely that the initially small and unfavourably oriented grains were first consumed by growing, favourably oriented grains before SSD progressed and led to the breakup of the film into isolated regions. In contrast, films deposited at elevated temperatures already exhibit larger grains and a more favourable texture in the as-deposited state. Furthermore, for films deposited above 100 °C, the dewetting

process can initiate at pre-existing voids, whereas films deposited at RT or 50 °C are initially continuous. If voids must first form via grain boundary grooving during the SSD process, as is the case in closed films, film breakup is delayed compared to films where voids are already present and merely expand. This delay allows for more extensive grain growth prior to the onset of SSD in the low-temperature-deposited films. In contrast, SSD can proceed further in the same time frame in films deposited at elevated temperatures, likely limiting additional grain growth. As a result, the particles formed from films deposited at higher temperatures are more equilibrated and it may also contribute to their smaller particle size.

However, the fact that the particles evolving from the film deposited at 250° C are not strongly faceted, in a different way from the Au films deposited at 100° C to 200° C, highlights that these particles are still related to the initial film (Figure 39 c)). In Figure 39 d) the change in covered area before and after post-annealing (Δ covered area = covered area before post-annealing – covered area after post-annealing) depending on the deposition temperature of the film is presented. It is noticeable that the change in covered are decreases with increasing deposition temperature. As noted earlier, the pre-existing voids are expected enable faster dewetting. However, the decrease in change of the covered are and the visible resemblance between the film deposited at 250° C and the corresponding particles, could also indicate an increase in thermal stability of the film with increasing deposition temperature. This could be due to a more energetically favourable initial state of the film (larger gain size, fibre texture) slowing the dewetting kinetics even though pre-existing voids are present.

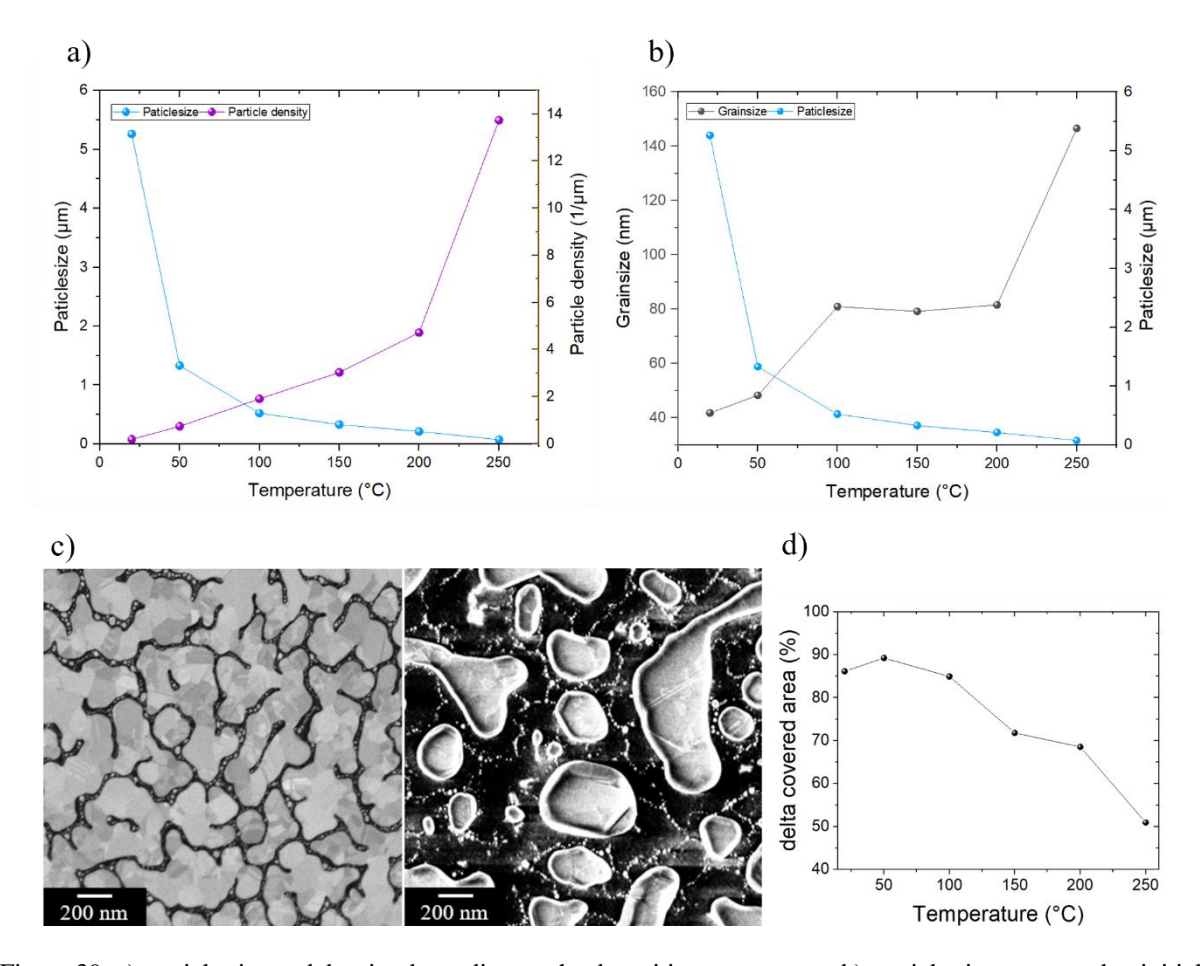


Figure 39: a) particle size and density depending on the deposition temperature b) particle size compared to initial grain size of as-dep film; the particle size decreases while the particle density increases with increasing initial deposition temperature and grain size, indicating that the grain size here is not the determining factor for the particle size c) BSE image of Au on sapphire deposited at 250°C and SE images after post-annealing at the same magnification, the particles evolved from the separated island in the as-deposited film, leading to the assumption that the pre-existing voids influence the particle size d) Δ covered area (covered area before post-annealing – covered area after post-annealing) before and after post-annealing decreases indicating an increase in thermal stability of the film at 800°C.

Lansaker et al. [21] compared the effects of heating during deposition and post-annealing of thin sputtered Au films. At RT deposition the film is not closed. Interestingly, the morphology that evolves from heating during deposition exhibits noticeably smaller structures whereas post-annealing leads to larger islands and voids. Although the microstructure was not analysed in detail in this study, the observed behaviour aligns well with the findings presented here. Heating during deposition, leads to fewer nuclei, which below a certain film thickness cannot coalesce into a continuous film. This results in the formation of smaller islands at higher temperatures instead of a closed film. In contrast, during post-annealing, SSD occurs, whereby voids either form or, as in this case, pre-existing voids grow as the film continues to retract. These observations indicate the presence of two distinct mechanisms leading to different microstructural outcomes. When both approaches are combined, as done in this study, heating

during deposition can be used strategically to tailor the particle size after post-annealing or to reduce the required annealing time, since larger defects are already present in the film.

The EBSD measurements of the post-annealed samples presented in Figure 33 show that the particles on all samples have a (111) fibre texture which is independent of the initial deposition temperature of the film which corresponds to literature [34].

The particles on the substrate lead to shadowing effects which is why data points with a low confidence index after spherical indexing are excluded. With increasing particle density, the shadowing gets worse which is why more data points need to be excluded. This leads to poor quality of the measurements, especially of the 250°C sample.

Summing up, the post-annealing experiments of Au films on sapphire indicate an enhanced thermal stability of the as-deposited film at higher deposition temperatures; even though the films are not closed due to an increase of the critical thickness with increasing deposition temperature. The increasing critical thickness leads to smaller particles after SSD as the process starts at pre-existing defects whereas the initial grain size of the as-deposited film is not a dominant factor if there are pre-existing voids in the film. Generally, the particle size can be tuned by changing the deposition temperature.

5.3.2 Au on ZnO

At 800 °C, the microstructure of Au films deposited on ZnO at varying temperatures exhibits distinct temperature-dependent phenomena. In contrast to sapphire substrates, the particle and grain sizes of post-annealed Au films on ZnO increase with deposition temperature, reflecting the influence of the initial grain size. The observation of particles at lower deposition temperatures and a mostly continuous film at higher deposition temperatures suggests that the thermal stability of Au thin films improves with increasing substrate temperature during deposition. Additionally, the deposition temperature significantly affects the texture evolution of the films, which correlates with the morphology observed after annealing. Finally, the microstructure of the as-deposited films governs the dewetting mechanisms that occur during post-annealing.

Figure 40 a) compares the initial grain size of the as-deposited samples with the particle size and grain size of the post-annealed films. In contrast to sapphire, the particle size on ZnO increases with increasing initial grain size for the RT and 50 °C samples, even though the as-deposited microstructures on both substrates are comparable. The film deposited at 100 °C and annealed at 800 °C exhibits a mixed morphology consisting of closed islands and dewetted areas; therefore, neither a particle nor a grain size can be reliably determined. For deposition temperatures of 150 °C and 200 °C, the grain size of the post-annealed films is significantly larger than that of the as-deposited ones. At 250 °C, however, both the as-deposited and post-annealed grain sizes decrease compared to lower deposition temperatures. As with Au on sapphire, the surface coverage of the Au films after annealing generally increases with increasing deposition temperature as presented in Figure 40 b).

As discussed previously for the as-deposited Au films on ZnO, the epitaxial relationship that forms at elevated deposition temperatures plays a crucial role in the microstructure evolution during film growth and it also influences the microstructural changes occurring during annealing at 800 °C. At RT and 50 °C, the Au films exhibit no preferred in-plane orientation or abnormal grain growth. Consequently, the films evolve into particles via SSD mechanism and exhibit a (111) fibre texture like the Au films on sapphire. However, the particles formed at RT are smaller than those at 50 °C. Since the film morphology is similar to that on sapphire but the particle size evolves differently, this suggests that the ZnO substrate has an additional influence on the morphology, independent of the overall film structure.

At a deposition temperature of 100 °C, the film consists of large islands with orientation relationship OR1 and dewetted finger-like regions with OR2. The as-deposited film is mainly characterized by OR2, but a few OR1 grains are also present. The mean grain size is 94 nm, and no twin boundaries are observed. At 800 °C, OR1 is expected to be present and abnormal grain growth is expected for OR1 grains [35]. This is consistent with the observation that OR1 grains remain as large, continuous islands after annealing. In contrast, areas exhibiting OR2 undergo dewetting, which indicates that OR2 is less stable at elevated temperatures. A comparison of the microstructure and texture before and after annealing suggests that grains

oriented in OR1 have grown significantly at 800 °C due to their energetic favourability. However, since OR2 was the dominant orientation in the as-deposited film and only a few grains exhibited OR1, OR2 remains dominant even after annealing. OR2 grains do not undergo abnormal growth; instead, they dewet. This behaviour may also be attributed to the higher grain boundary energies associated with grains in the as-deposited film.

Au films deposited at 150 °C, 200 °C, and 250 °C exhibit exclusively OR2 after post-annealing. These films remain largely continuous with some holes, and their grain sizes are significantly larger than in the as-deposited state. At first glance, this seems to contradict the findings for the 100 °C sample, where OR2 underwent dewetting. However, a more detailed analysis of the as-deposited microstructures reveals that already here a mazed bicrystal microstructure was present, and the grain boundaries consisted mainly of low-energy configurations such as twin or low-angle boundaries.

These findings suggest that a reorientation from OR2 to OR1 is unlikely. This interpretation is supported by the 100 °C sample, where OR1 was already present in the as-deposited state and thus capable of growing during annealing. Furthermore, the presence of abnormally large grains and energetically favourable grain boundaries in the 150 to 250 °C samples suppress SSD. Atiya et al. [26] reported that abnormal grains hinder the dewetting process. This observation aligns with the fact that films exhibiting abnormal grain growth in the as-deposited state remain continuous after annealing at 800 °C. Nevertheless, the presence of holes suggests that grain growth in OR2 grains does not completely prevent dewetting. Grain growth and SSD appear to be competing processes at elevated temperatures. In the 100 °C sample, SSD was dominant in OR2 grains, while OR1 grains grew. Reports in the literature show that OR1 grains forming at 800 °C typically do not undergo dewetting, further supporting the notion that OR2 is thermally less stable [35]. However, at deposition temperatures of 150 °C and above, the as-deposited microstructure is already sufficiently stable such that epitaxy-driven grain growth substantially slows the dewetting process.

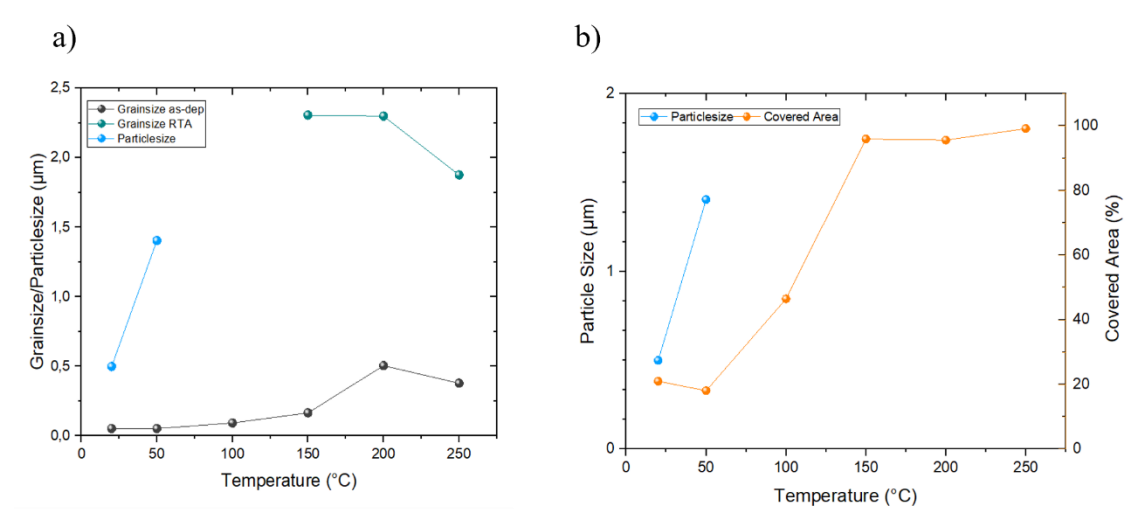


Figure 40: a) Initial grain size compared to particle size/grain size after post-annealing of Au on ZnO b) Particle size and covered are of post-annealed Au on ZnO films. The particle size (RT, 50° C) and grain size (> 100° C) increases, the grain size after post-annealing is significantly larger than the as-deposited grain size. The covered area increases with initial deposition temperature, indicating a higher thermal stability, especially when abnormal OR2 oriented grains were already present in the as-deposited film (films deposited at 150° C and above).

A closer examination of the holes in the 150 °C, 200 °C, and 250 °C samples, as shown in Figure 41 a), reveals distinct morphological differences. SE images of holes in each sample show that the 150 °C and 200 °C films feature pronounced raised rims surrounding the holes. This characteristic morphology is typical of classical SSD, where material is redistributed away from the hole via surface diffusion and accumulates at the edges[8]. The presence of raised rims is therefore a clear indicator of SSD activity driven by surface self-diffusion. The nucleation of holes is likely defect-driven, as small voids are already present in the as-deposited films. These pre-existing defects may have acted as initiation sites for dewetting during annealing at 800 °C. Fewer small spherical holes are observed in the 150 °C sample compared to the 200 °C film, resulting in the formation of fewer but larger holes in the former and more, smaller holes in the latter. Since grain boundaries in these films are mainly twin and low-angle boundaries, which are energetically stable, hole nucleation at grain boundaries is unlikely.

In contrast, the 250 °C as-deposited film does not exhibit spherical holes like the 150 °C and 200 °C films. After annealing, the film contains significantly smaller holes without raised rims. Furthermore, hillocks are visible on the surface, as shown in Figure 41 b). These two observations suggest that dewetting in this case proceeds via a different mechanism, not driven by surface self-diffusion. Rather, mass transport likely occurs through alternative paths such as interfacial diffusion along the film–substrate interface or via grain boundary diffusion. Consequently, no raised rims form; instead, the redistributed material accumulates at some distance from the hole edge, forming hillocks [23], [24], [25].

The formation of holes in thin films without raised rims has been addressed in several studies. Shaffir et al. [24] demonstrated that this dewetting mechanism occurs when the interface

energy exceeds the surface energy. Their study found that hole nucleation in such cases does not occur at grain boundaries or surface defects, but rather at triple junctions at the film—substrate interface. Cross-sectional analysis revealed that holes grow upward from the interface, with voids located at the film—substrate interface.

For the 250 °C sample, no pre-existing holes are visible in the as-deposited film that could serve as precursors for SSD during annealing at 800 °C. In addition, grain boundary grooving is unlikely due to the prevalence of low energy grain boundaries and abnormal grains. The epitaxial nature of the film contributes to its structural stability. Thus, it is plausible that the energetically least favourable sites for hole nucleation are located at the interface.

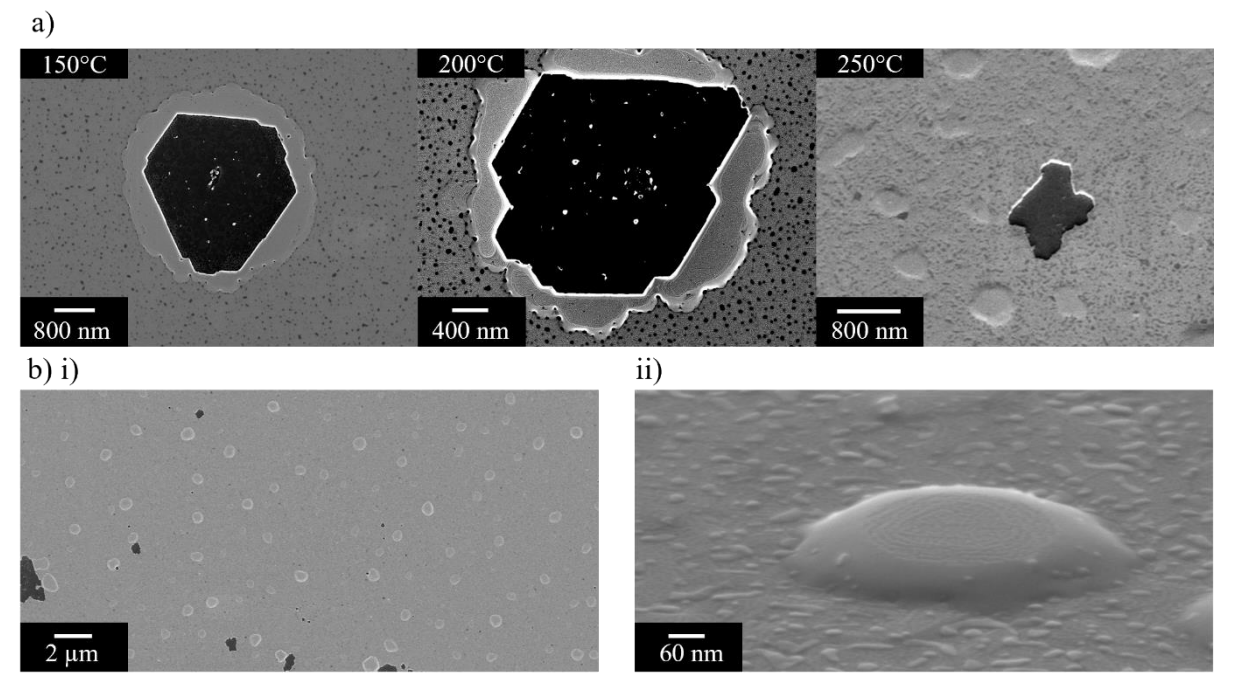


Figure 41: SEM images of a) holes in Au on ZnO after post-annealing deposited at 150°C and 200°C with rims and 250°C without rims, indicating the presence of different dewetting mechanisms. The holes with rims are typical for dewetting via self-surface diffusion whereas the absence of rims indicate dewetting via interface diffusion b) hillocks on Au on ZnO deposited at 250°C after post-annealing i) overview ii) higher magnification; hillocks are typically observed with holes without rims and therefore indicate dewetting via interface diffusion as well.

To investigate this further, a cross-sectional lamella of the post-annealed Au film deposited at 250 °C was analysed using STEM, as shown in Figure 42. Figure 42 a) presents an overview image. The average film thickness is 39 nm, excluding the hillocks, confirming that the film thickness remains unchanged after annealing. Voids are visible at the film—substrate interface, including a large central hole that nearly penetrates the entire film, as well as additional holes beneath the hillocks. In Figure 42 b), the film thickness at the edge of a large hole is measured to be 40 nm, confirming the absence of a raised rim, which correlates with the presence of hillocks and interfacial voids. The large number of interfacial voids explains the extensive

hillock formation observed on the film surface. The hillock analysed in Figure 42 c) has a diameter of 455 nm and a height of 38 nm relative to the original film thickness. An interface between the hillock and the underlying film is also visible.

The STEM analysis thus confirms that a dewetting mechanism similar to that described by Shaffir et al. [24] is active in the 250 °C sample. Voids nucleate at the film–substrate interface, and material diffuses along this interface or along grain boundaries, subsequently agglomerating as hillocks on the film surface.

The hypothesis that the interface energy is higher than the surface or grain boundary energy is supported by analysis of the 200 °C as-deposited cross-section, where voids are also observed at the interface even before annealing. However, while the as-deposited film of the 250 °C sample exhibits pronounced surface grooves (Figure 36 b)), annealing results in a smooth surface with interfacial voids. This suggests that the film is fully closed at 800 °C before or concurrently with the onset of dewetting, again indicating a competition between grain growth and dewetting in this system. This conclusion is consistent with the observation that the grain size both before and after annealing is smaller in the 250 °C sample compared to the 200 °C sample.

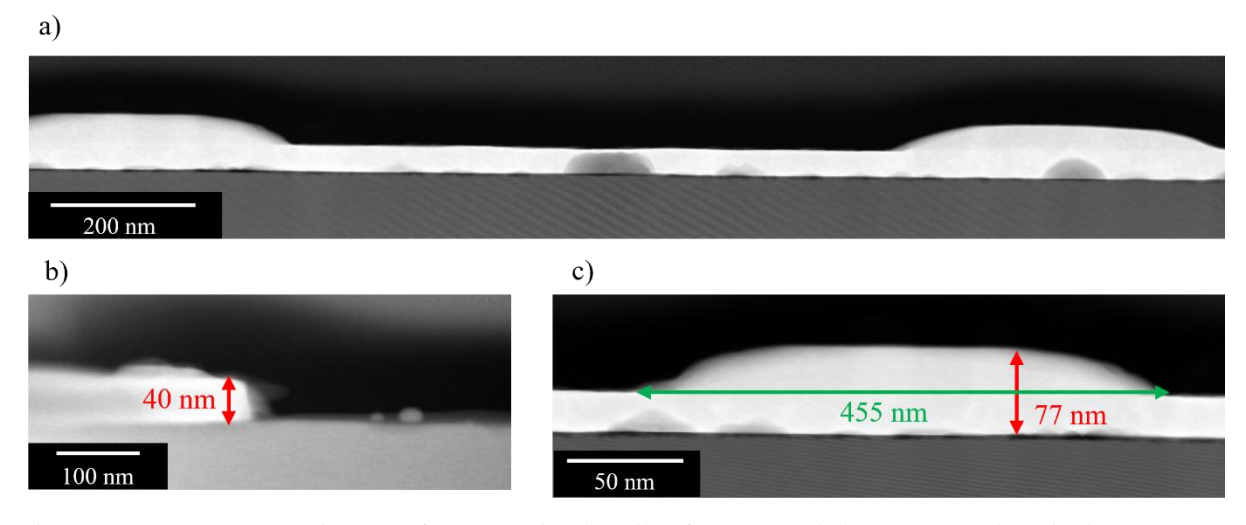


Figure 42: HAADF STEM images of cross-section lamella of post-annealed Au on ZnO deposited at 250°C a) overview with hillocks and holes forming at the interface b) film at the edge of a hole c) close up of a hillock. The cross-section confirms the absence of rims around the holes and the hole formation at the interface, typically observed with hillocks. The appearance of this alternative dewetting mechanism could indicate that the interface energy is higher than the surface energy, leading to hole nucleation and material transport at the interface, not the surface.

5.3.3 Substrate reaction ZnO with Au thin film

In the Au films deposited on ZnO at temperatures between 150 °C and 250 °C, post-annealing at 800 °C results in the appearance of dark particles in SEM images, visible in both SE and BSE modes (Figure 43 a)). In the sample deposited at 150 °C, large particles can be observed at the edges of some holes, while smaller particles are present across all samples all over the films. The fact that these particles appear dark in BSE imaging suggests that they are not composed of gold. To investigate this, EDX measurements are carried out in the SEM on the 150 °C sample, presented in Figure 43 b).

Point analyses are performed on a large particle at the edge of a hole, on the gold film and on the exposed substrate within the void. The measurements show clear signals of Au, Zn, and O at the particle, whereas the Zn peak is barely visible on the Au film. On the exposed substrate, only Zn and O are detected. These results clearly indicate that the substrate has reacted with the Au film, and that Zn or ZnO has diffused through the film and accumulated on its surface. However, according to the literature, ZnO is considered stable in contact with gold at 800 °C in nitrogen atmosphere [35].

Comparing the exposed substrate areas in the dewetted samples deposited at room temperature, 50 °C, and 100 °C (Figure 43 c)) reveals that the substrate appears porous in all cases, indicating a chemical reaction may have occurred there as well. Moreover, the degree of substrate degradation increases from RT to 100 °C, with a higher density of holes observed at elevated deposition temperatures. This suggests that the deposition temperature may influence the reactivity between Au and ZnO during subsequent annealing at 800 °C. Alternatively, it is also possible that the interface had already reacted prior to annealing, though this cannot be confirmed, as the substrate is completely covered in the as-deposited films.

However, Dierner et al. [35] did not report any reaction after annealing the exact same material system at 800°C. Given that the substrate deposited at room temperature exhibits only limited signs of degradation after post-annealing, it is conceivable that such effects remained undetected in the previous study.

Given the observed reaction, it is plausible that some of the phenomena observed in the system such as texture development and dewetting are influenced by this interfacial interaction. Consequently, some of the assumptions regarding the influence of the substrate temperature on the behaviour of Au on ZnO may not hold true in light of the reactivity between the two materials.

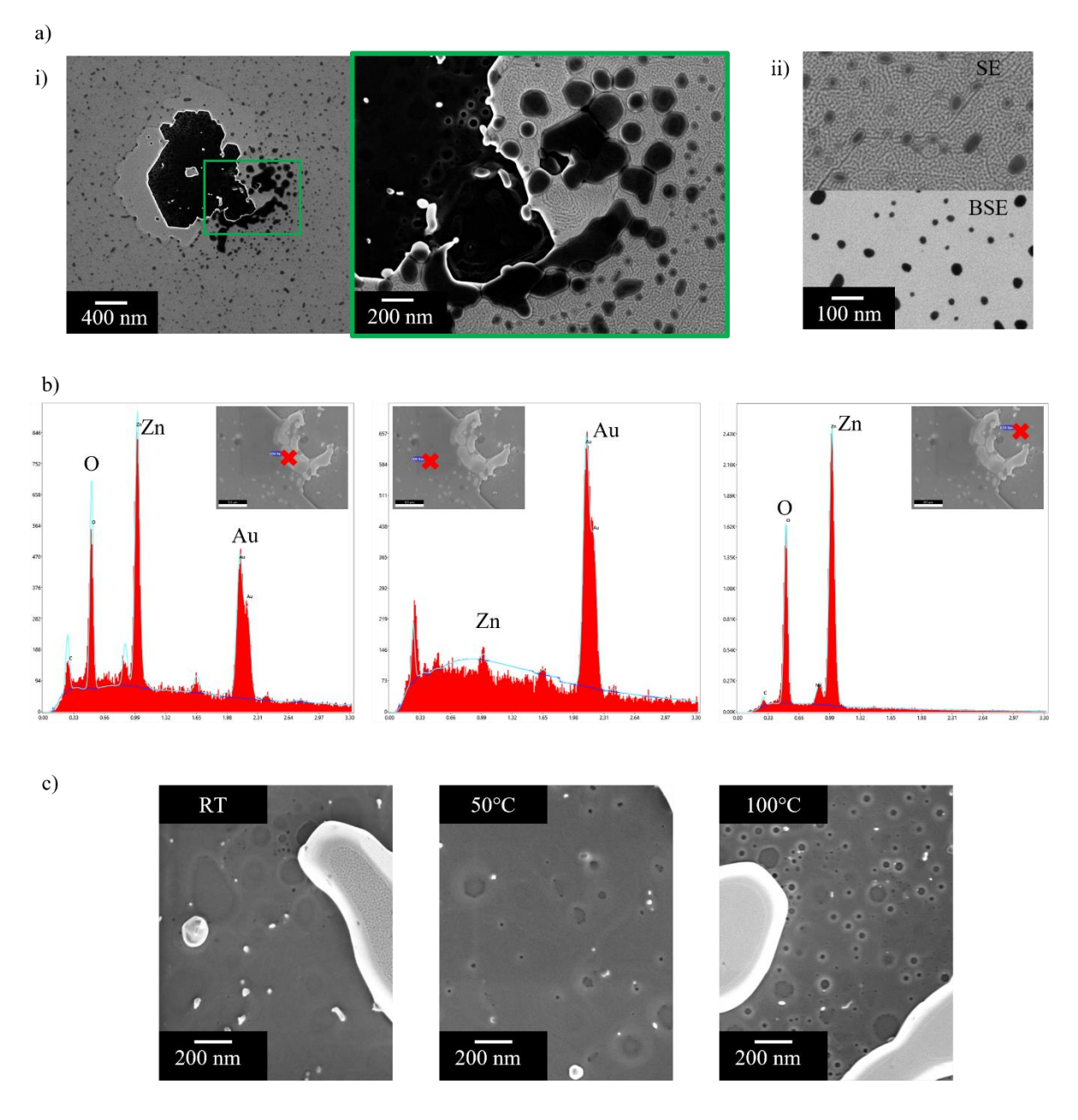


Figure 43: a) SEM images of particles on Au surface i) at the edge of a large hole b) on the film; the particles appear darker than the film in SE and BSE mode indicating a different chemical composition b) EDX point measurements on a particle, the substrate and the Au film clearly show a higher Zn peak on the particle than on the film c) Substrate after post-annealing of Au films deposited at RT, 50°C and 100°C; the substrate surface is clearly damaged and the damage increases with increasing initial deposition temperature.

5 Conclusion and Outlook

This work set out to determine how substrate temperature impacts thin film growth and, in turn, the resulting microstructure. The findings reveal a clear interplay between deposition conditions and the as-deposited film properties, but also highlight how these initial states influence the film's thermal stability and morphological evolution upon annealing at 800 °C. On both sapphire and ZnO substrates, increasing the deposition temperature leads to a noticeable enlargement of grain size and a more uniform grain structure. This behaviour is consistent with the structure zone model, indicating a transition to Zone 2, characterized by competitive grain growth and enhanced surface diffusion, occurring already at approximately 150 °C. On sapphire, the grains exhibit a pronounced (111) fibre texture, which becomes more distinct with increasing temperature. However, the films are not closed showing increasingly larger voids at elevated deposition temperatures, suggesting a higher critical thickness required for continuous film formation. On ZnO, a different trend is observed. At deposition temperatures above 100 °C, a strong orientation relationship OR2 emerges, which promotes abnormal grain growth. This grain growth behaviour appears to support the formation of more continuous films compared to sapphire under similar conditions, indicating a lower critical thickness on ZnO. Nevertheless, small spherical voids are still observable at 150 °C and 200 °C. Notably, the film deposited at 200 °C exhibits hourglass-shaped holes, suggesting that coalescence of growing islands occurs in the middle of the film thickness, rather than at the substrate interface or the surface. This mechanism likely contributes to the deep surface grooves observed in these films.

Thermal annealing at 800 °C serves as a key method to evaluate the thermal stability and transformation pathways of the as-deposited microstructures. On sapphire, all samples transform into nanoparticle structures after annealing. Interestingly, the particle size decreases with increasing deposition temperature, likely due to the presence of pre-existing voids in the as-deposited films boosting SSD kinetics. Despite this, the thermal stability improves with deposition temperature; for instance, the grain structure of the film deposited at 250 °C remains partially intact after annealing.

In contrast, Au films on ZnO demonstrate a more complex evolution. Films deposited at low temperatures tend to dewet and form particles or isolated islands after annealing. At higher deposition temperatures (>100 °C), the films remain largely continuous, with only occasional large holes, indicating enhanced thermal stability, greater even than that observed on sapphire for similarly deposited films. The resulting particles also exhibit a (111) fibre texture similar to those on sapphire. The film deposited at 100 °C features large islands with OR1 and finger-like dewetted structures with OR2, implying that OR1 is the energetically preferred orientation. However, films that initially exhibited OR2 and abnormal grain growth retain this orientation after annealing and do not undergo dewetting. This behaviour likely results from the stability of the abnormally large grains and the associated low-energy grain boundaries.

A particularly distinct behaviour is observed in the Au film deposited on ZnO at 250 °C. Post-annealing results in the formation of hillocks, and the absence of rims around the large holes, along with interfacial hole formation, suggests an alternative dewetting mechanism. Rather than surface diffusion, the dominant mass transport mechanism appears to be grain boundary or interfacial diffusion. This implies that the film's defects are energetically unfavourable at the interface, especially given the absence of pre-existing voids prior to annealing.

A further complication is the apparent reaction between Au and ZnO upon annealing. The ZnO substrate appears porous post-annealing, and Zn or ZnO-rich particles are observed on the surface of the Au films. While the exact role of this reaction in influencing film behaviour is not yet fully understood, it may have contributed to some of the phenomena observed on ZnO.

To gain deeper insight into the growth and dewetting behaviour of Au thin films on sapphire and ZnO, further studies are essential. Improved control and precise calibration of the substrate temperature during e-beam deposition are critical to ensure reproducibility and reliability. A systematic thickness series could offer valuable information on the transition between different film growth regimes and help to capture early-stage morphological changes.

Moreover, varying annealing parameters such as temperature and time will allow a more detailed understanding of how the as-deposited microstructure governs subsequent thermal evolution. In-situ heating experiments could provide real-time data on morphological and crystallographic transformations during annealing.

Overall, Substrate heating during deposition presents a versatile and easily implemented parameter to tune the film microstructure and its thermal stability. As such, it is a highly promising tool that merits further investigation, both to understand fundamental mechanisms and to optimize thin film properties for targeted applications.

References

- [1] R. Malabi *et al.*, "Growth and characterisation of gold thin film layer using an ebeam evaporation system for surface plasmon resonance applications," in *Plasmonics in Biology and Medicine XVI*, T. Vo-Dinh, H.-P. A. Ho, and K. Ray, Eds., SPIE, Mar. 2019, p. 49. doi: 10.1117/12.2509972.
- [2] C. V. Thompson, "Structure Evolution During Processing of Polycrystalline Films," *Annual Review of Materials Science*, vol. 30, no. 1, pp. 159–190, Aug. 2000, doi: 10.1146/annurev.matsci.30.1.159.
- [3] Z. Wang and Z. Zhang, "Electron Beam Evaporation Deposition," in *Advanced Nano Deposition Methods*, Wiley, 2016, pp. 33–58. doi: 10.1002/9783527696406.ch2.
- [4] O. O. Abegunde, E. T. Akinlabi, O. P. Oladijo, S. Akinlabi, and A. U. Ude, "Overview of thin film deposition techniques," 2019, *AIMS Press*. doi: 10.3934/MATERSCI.2019.2.174.
- [5] M. Levlin, A. Laakso, E.-M. Niemi, and P. Hautojarvï, "Evaporation of gold thin films on mica: effect of evaporation parameters," 1997.
- [6] M. V. Belous and C. M. Wayman, "Temperature changes in thin metal films during vapor deposition," *J Appl Phys*, vol. 38, no. 13, pp. 5119–5124, 1967, doi: 10.1063/1.1709287.
- [7] F. Leroy *et al.*, "How to control solid state dewetting: A short review," Jun. 01, 2016, *Elsevier*. doi: 10.1016/j.surfrep.2016.03.002.
- [8] C. V. Thompson, "Solid-state dewetting of thin films," Aug. 2012. doi: 10.1146/annurey-matsci-070511-155048.
- [9] M. Altomare, N. T. Nguyen, and P. Schmuki, "Templated dewetting: designing entirely self-organized platforms for photocatalysis," *Chem Sci*, vol. 7, no. 12, pp. 6865–6886, 2016, doi: 10.1039/C6SC02555B.
- [10] J. Ye, D. Zuev, and S. Makarov, "Dewetting mechanisms and their exploitation for the large-scale fabrication of advanced nanophotonic systems," 2019, *Taylor and Francis Ltd.* doi: 10.1080/09506608.2018.1543832.
- [11] S. Harsha *et al.*, "Dewetting of Pt Nanoparticles Boosts Electrocatalytic Hydrogen Evolution Due to Electronic Metal-Support Interaction," *Adv Funct Mater*, Oct. 2024, doi: 10.1002/adfm.202403628.

- [12] N. Haustrup and G. M. O'Connor, "The influence of thin film grain size on the size of nanoparticles generated during UV femtosecond laser ablation of thin gold films," *Appl Surf Sci*, vol. 278, pp. 86–91, Aug. 2013, doi: 10.1016/j.apsusc.2012.10.201.
- [13] N. Kaiser, "Review of the fundamentals of thin-film growth," *Appl Opt*, vol. 41, no. 16, p. 3053, Jun. 2002, doi: 10.1364/AO.41.003053.
- [14] G. G. Sumner, "Effects of substrate temperature on the growth of thin platinum deposits on rock salt," *Philosophical Magazine*, vol. 12, no. 118, pp. 767–775, 1965, doi: 10.1080/14786436508218915.
- [15] K. L. Chopra and M. R. Randlett, "Influence of deposition parameters on the coalescence stage of growth of metal films," *J Appl Phys*, vol. 39, no. 3, pp. 1874–1881, 1968, doi: 10.1063/1.1656444.
- [16] Y. Golan, L. Margulis, and I. Rubinstein, "Vacuum-deposited gold films," *Surf Sci*, vol. 264, no. 3, pp. 312–326, Mar. 1992, doi: 10.1016/0039-6028(92)90188-C.
- [17] B. A. D. A. V Movchan, "STRUCTURE AND PROPERTIES OF THICK CONDENSATES OF NICKEL, TITANIUM, TUNGSTEN, ALUMINUM OXIDES, AND ZIRCONIUM DIOXIDE IN VACUUM," *Fiz. Metal. Metalloved.*, vol. 28, pp. 653–660, 1969.
- [18] J. A. Thornton, "High Rate Thick Film Growth," *Annual Review of Materials Science*, vol. 7, no. 1, pp. 239–260, Aug. 1977, doi: 10.1146/annurev.ms.07.080177.001323.
- [19] R. Messier, A. P. Giri, and R. A. Roy, "Revised structure zone model for thin film physical structure," *Journal of Vacuum Science & Technology A: Vacuum, Surfaces, and Films*, vol. 2, no. 2, pp. 500–503, Apr. 1984, doi: 10.1116/1.572604.
- [20] C. R. M. Grovenor, H. T. G. Hentzell, and D. A. Smith, "The development of grain structure during growth of metallic films," *Acta Metallurgica*, vol. 32, no. 5, pp. 773–781, May 1984, doi: 10.1016/0001-6160(84)90150-0.
- [21] P. C. Lansåker, G. A. Niklasson, and C. G. Granqvist, "Thin gold films on SnO 2:In: Temperature-dependent effects on the optical properties," *Thin Solid Films*, vol. 520, no. 9, pp. 3688–3691, Feb. 2012, doi: 10.1016/j.tsf.2012.01.016.
- [22] P. Jacquet *et al.*, "On the solid-state dewetting of polycrystalline thin films: Capillary versus grain growth approach," *Acta Mater*, vol. 143, pp. 281–290, Jan. 2018, doi: 10.1016/j.actamat.2017.08.070.
- [23] O. Kovalenko, J. R. Greer, and E. Rabkin, "Solid-state dewetting of thin iron films on sapphire substrates controlled by grain boundary diffusion," *Acta Mater*, vol. 61, no. 9, pp. 3148–3156, May 2013, doi: 10.1016/j.actamat.2013.01.062.

- [24] E. Shaffir, I. Riess, and W. D. Kaplan, "The mechanism of initial de-wetting and detachment of thin Au films on YSZ," *Acta Mater*, vol. 57, no. 1, pp. 248–256, Jan. 2009, doi: 10.1016/j.actamat.2008.09.004.
- [25] W. D. Kaplan, D. Chatain, P. Wynblatt, and W. C. Carter, "A review of wetting versus adsorption, complexions, and related phenomena: The rosetta stone of wetting," Sep. 2013. doi: 10.1007/s10853-013-7462-y.
- [26] G. Atiya, D. Chatain, V. Mikhelashvili, G. Eisenstein, and W. D. Kaplan, "The role of abnormal grain growth on solid-state dewetting kinetics," *Acta Mater*, vol. 81, pp. 304–314, Dec. 2014, doi: 10.1016/j.actamat.2014.08.038.
- [27] C. M. Müller and R. Spolenak, "Microstructure evolution during dewetting in thin Au films," *Acta Mater*, vol. 58, no. 18, pp. 6035–6045, 2010, doi: 10.1016/j.actamat.2010.07.021.
- [28] "AS-One 100 Rapid Thermal Processor User's manual Document Title Version Date of Issue Filename Rapid Thermal Processor AS-One 100-User's Manual."
- [29] L. Vitos, A. V Ruban, H. L. Skriver, and J. Kollár, "The surface energy of metals," 1998.
- [30] A. E. Muslimov, A. V. Butashin, A. B. Kolymagin, V. P. Vlasov, and V. M. Kanevsky, "Epitaxy of gold films on the structured (0001) sapphire surface," *Crystallography Reports*, vol. 60, no. 6, pp. 942–945, Nov. 2015, doi: 10.1134/S1063774515060218.
- [31] G. Kästle, H.-G. Boyen, B. Koslowski, A. Plettl, F. Weigl, and P. Ziemann, "Growth of thin, flat, epitaxial () oriented gold films on c-cut sapphire," *Surf Sci*, vol. 498, no. 1–2, pp. 168–174, Feb. 2002, doi: 10.1016/S0039-6028(01)01685-5.
- [32] H. Sadan and W. D. Kaplan, "Au-Sapphire (0001) solid-solid interfacial energy," in *Journal of Materials Science*, Aug. 2006, pp. 5099–5107. doi: 10.1007/s10853-006-0437-5.
- [33] O. Malyi, L. Klinger, D. J. Srolovitz, and E. Rabkin, "Size and shape evolution of faceted bicrystal nanoparticles of gold on sapphire," *Acta Mater*, vol. 59, no. 7, pp. 2872–2881, Apr. 2011, doi: 10.1016/j.actamat.2011.01.030.
- [34] D. Amram and E. Rabkin, "On the role of Fe in the growth of single crystalline heteroepitaxial Au thin films on sapphire," *Acta Mater*, vol. 61, no. 11, pp. 4113–4126, Jun. 2013, doi: 10.1016/j.actamat.2013.03.038.

- [35] M. Dierner *et al.*, "Influence of substrate polarity on thermal stability, grain growth and atomic interface structure of Au thin films on ZnO surfaces," *Acta Mater*, vol. 284, Jan. 2025, doi: 10.1016/j.actamat.2024.120531.
- [36] W. Zhou, R. Apkarian, Z. L. Wang, and D. Joy, "Fundamentals of Scanning Electron Microscopy (SEM)," in *Scanning Microscopy for Nanotechnology*, New York, NY: Springer New York, 2006, pp. 1–40. doi: 10.1007/978-0-387-39620-0_1.
- [37] L. Reimer, *Scanning Electron Microscopy*, vol. 45. in Springer Series in Optical Sciences, vol. 45. Berlin, Heidelberg: Springer Berlin Heidelberg, 1998. doi: 10.1007/978-3-540-38967-5.
- [38] D. B. Williams and C. B. Carter, *Transmission Electron Microscopy*. Boston, MA: Springer US, 2009. doi: 10.1007/978-0-387-76501-3.
- [39] Electron Backscatter Diffraction in Materials Science. Springer US, 2000. doi: 10.1007/978-1-4757-3205-4.
- [40] F. J. Humphreys, "Review Grain and subgrain characterisation by electron backscatter diffraction." doi: 10.1023/A:1017973432592.
- [41] W. C. Lenthe, S. Singh, and M. De Graef, "A spherical harmonic transform approach to the indexing of electron back-scattered diffraction patterns," *Ultramicroscopy*, vol. 207, Dec. 2019, doi: 10.1016/j.ultramic.2019.112841.
- [42] A. J. Schwartz, M. Kumar, B. L. Adams, and D. P. Field, *Electron backscatter diffraction in materials science*. Springer US, 2009. doi: 10.1007/978-0-387-88136-2.
- [43] F. J. Giessibl, "Advances in atomic force microscopy," *Rev Mod Phys*, vol. 75, no. 3, pp. 949–983, Jul. 2003, doi: 10.1103/RevModPhys.75.949.
- [44] D. G. Yablon, "Overview of Atomic Force Microscopy," in *Scanning Probe Microscopy in Industrial Applications*, Wiley, 2013, pp. 1–14. doi: 10.1002/9781118723111.ch1.
- [45] Y. Seo and W. Jhe, "Atomic force microscopy and spectroscopy," *Reports on Progress in Physics*, vol. 71, no. 1, Jan. 2008, doi: 10.1088/0034-4885/71/1/016101.
- [46] R. Schneider, "Energy-Dispersive X-Ray Spectroscopy (EDXS)," in *Surface and Thin Film Analysis*, Wiley, 2011, pp. 293–310. doi: 10.1002/9783527636921.ch18.
- [47] N. Jedrecy, G. Renaud, R. Lazzari, and J. Jupille, "Unstrained islands with interface coincidence sites versus strained islands: X-ray measurements on Ag•ZnO," *Phys Rev B Condens Matter Mater Phys*, vol. 72, no. 19, Nov. 2005, doi: 10.1103/PhysRevB.72.195404.

- [48] A. Weinberg and J. David, "Thermodynamics of translational states in the Sigma 3 grain boundary system. Item Type text; Dissertation-Reproduction (electronic)." [Online]. Available: http://hdl.handle.net/10150/187219
- [49] "https://msestudent.com/what-does-bse-stand-for-backscattered-electron/ 08.05.2025."
- [50] A. D. Herron, S. P. Coleman, K. Q. Dang, D. E. Spearot, and E. R. Homer, "Simulation of kinematic Kikuchi diffraction patterns from atomistic structures," *MethodsX*, vol. 5, pp. 1187–1203, Jan. 2018, doi: 10.1016/j.mex.2018.09.001.

Eidesstattliche Erklärung

Ich versichere, dass ich die Arbeit ohne fremde Hilfsmittel und ohne Benutzung anderer als der angegebenen Quellen angefertigt habe und dass die Arbeit in gleicher oder ähnlicher Form noch keiner anderen Prüfungsbehörde vorgelegen hat und von dieser als Teil einer Prüfungsleistung angenommen wurde. Alle Ausführungen, die wörtlich oder sinngemäß übernommen wurden, sind als solche gekennzeichnet.

| Datum: | Unterschrift: | |
|--------|---------------|--|